ARL-TR-8923 ● MAR 2020

Optical Examination of Transparent Nanocomposites Using Near-Infrared Light Sources

by Donovan Harris

NOTICES

Disclaimers

The findings in this report are not to be construed as an official Department of the Army position unless so designated by other authorized documents.

Citation of manufacturer's or trade names does not constitute an official endorsement or approval of the use thereof.

Destroy this report when it is no longer needed. Do not return it to the originator.

ARL-TR-8923 ● MAR 2020

Optical Examination of Transparent Nanocomposites Using Near-Infrared Light Sources

Donovan Harris
Weapons and Materials Research Directorate, CCDC Army Research Laboratory

REPORT DOCUMENTATION PAGE

Form Approved
OMB No. 0704-0188

1. REPORT DATE *(DD-MM-YYYY)*	2. REPORT TYPE	3. DATES COVERED (From - To)
March 2020	Technical Report	2016–2018

4. TITLE AND SUBTITLE
Optical Examination of Transparent Nanocomposites Using Near Infrared Light Sources

5a. CONTRACT NUMBER

5b. GRANT NUMBER

5c. PROGRAM ELEMENT NUMBER

6. AUTHOR(S)
Donovan Harris

5d. PROJECT NUMBER

5e. TASK NUMBER

5f. WORK UNIT NUMBER

7. PERFORMING ORGANIZATION NAME(S) AND ADDRESS(ES)
CCDC Army Research Laboratory
ATTN: FCDD-RLW-ME
Aberdeen Proving Ground, MD 21005

8. PERFORMING ORGANIZATION REPORT NUMBER
ARL-TR-8923

9. SPONSORING/MONITORING AGENCY NAME(S) AND ADDRESS(ES)

10. SPONSOR/MONITOR'S ACRONYM(S)

11. SPONSOR/MONITOR'S REPORT NUMBER(S)

12. DISTRIBUTION/AVAILABILITY STATEMENT
Approved for public release; distribution is unlimited.

13. SUPPLEMENTARY NOTES

14. ABSTRACT
This optical near-infrared (NIR) report covers efforts attempting to use transmitted wideband monochromic NIR illumination in investigating the nature of globular-appearing inclusions in five erbium (Er): yttrium oxide–magnesium oxide nanocomposite specimens. Starting with the initial macro-image 1× findings, the report moves to discuss the chemistry and fluorescence generation of the nanocomposite ceramics examined. The microscope's hardware and software are then discussed. The test protocol section is brief. Results are divided into three sections, 850 nm, 850/780 nm, and 780 nm, with each specimen discussed separately. The issue of Er fluorescence and its imaging effects are noted. The summary attempts to identify common findings for both NIR wavelengths and discuss major differences. Conclusion discussions address the changes in initial premises and the utility of transmitted NIR in ceramics characterization.

15. SUBJECT TERMS
transparent ceramic nanocomposites, infrared transmission, optical microscopy, microstructure, near-infrared

16. SECURITY CLASSIFICATION OF:			17. LIMITATION OF ABSTRACT	18. NUMBER OF PAGES	19a. NAME OF RESPONSIBLE PERSON
a. REPORT	b. ABSTRACT	c. THIS PAGE			Victoria Blair
Unclassified	Unclassified	Unclassified	UU	72	19b. TELEPHONE NUMBER (Include area code) (410) 306-4947

Contents

List of Figures

List of Tables

1. Introduction and Background

In a 2018 report by the US Army Research Laboratory (ARL), Fleischman et al.[1] sought to develop an improved nanocomposite laser host material possessing improved thermal, luminescence, and phonon energy properties. As these materials are intended for use as a mid-IR laser gain material, they have erbium (Er) doped into the yttrium oxide (Y_2O_3) phase, which behaves as the lasing active ion. Figure 1 shows the energy levels of Er within a Y_2O_3 host lattice. In the case of Er, there are several photon transitions that are possible: $^4I_{11/2}$ to $^4I_{13/2}$, which emits at 2700 nm, and $^4I_{13/2}$ to $^4I_{15/2}$, which emits at 1600 nm. Typically, a light source at a wavelength of 980 nm is used to probe the $^4I_{11/2} > {}^4I_{13/2}$ transition, but a light source set to 800 nm can easily activate the $^4I_{13/2}$ to $^4I_{15/2}$ transition. Therefore, the 1600-nm emission is likely to interfere with imaging using the near-infrared (NIR) camera if a sufficient concentration of erbium is in the specimen.

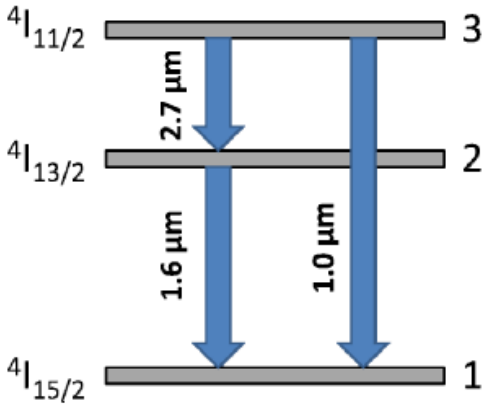

Fig. 1 Diagram of energy levels of Er^{3+}:Y_2O_3 showing emission wavelengths when the material is excited by a probing light source

Macrographs at 1× magnification to document nine nanocomposite ceramics for the ARL report[1] were made using transmitted white light and a digital single lens reflex (DSLR) camera with a 105-mm macro lens. The resulting macrographs revealed what appeared to be inclusions of various sizes, examples of which are shown in Fig. 2. To the eye, these specimens appear opaque, the result of any reflected light being randomly scattered by the nano-arrayed phases. The presence of apparently subsurface features prompted the questions, 1) Will they interfere with the in-line transmission of NIR laser beam and 2) Can their structure be resolved optically? ARL's Ceramic and Transparent Materials Branch of the Weapons and Materials Research Directorate possessed an optical microscope system configured to perform subsurface grain studies of transparent ceramics, which became the designated analytic tool to resolve those questions.

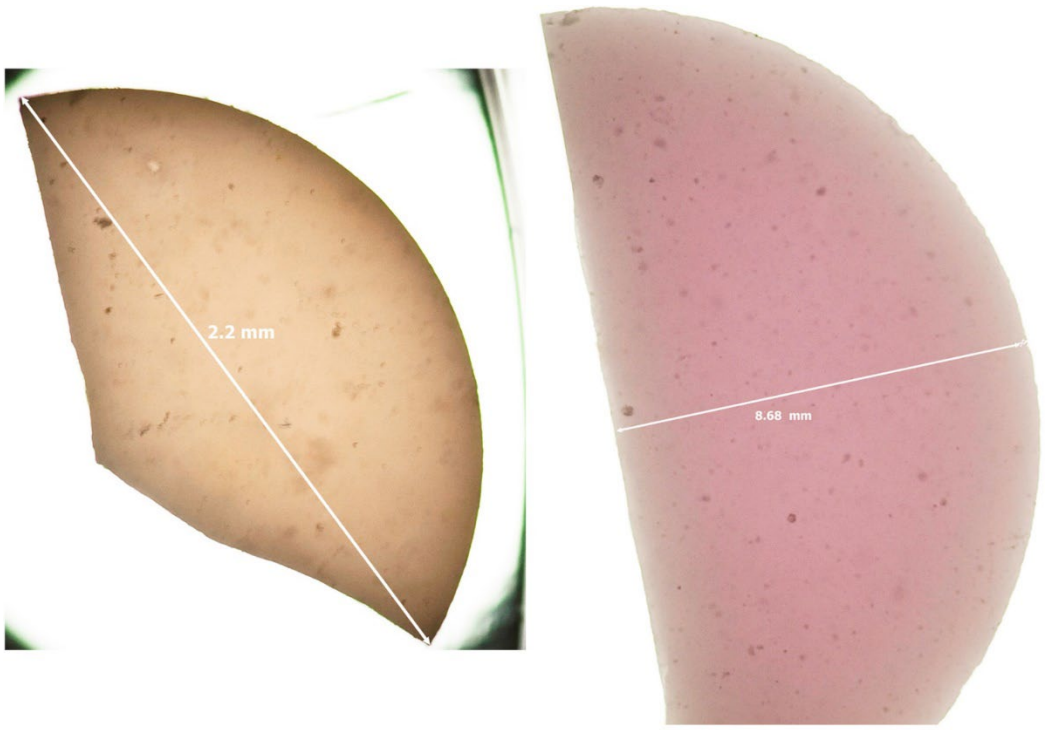

Fig. 2 Macro 1× transmitted light images of two transparent ceramics: (left) 1VB124, a composite of Er:Y_2O_3 and magnesium oxide (MgO), and (right) 4CC, a single-phase Er:MgO

This report covers optical microscopy of a series of Er:Y_2O_3–MgO nanocomposite ceramic formulations using both visible and NIR illumination to identify the nature of the apparent subsurface occlusions. It was also desired to determine if the apparent subsurface occlusions could interfere with transmitted NIR.

A Zeiss Z2m compound optical microscope using AxioVision 4.9 software was used throughout the study. Not possessing instruments capable of NIR laser imaging, available compatible NIR LEDs became the potential illuminant sources at 940 nm, 850 nm, and 780nm. The 940-nm light source was ultimately unable to provide any satisfactory images.

Experimental and test protocols including material synthesis, instrumentation, and test procedure is presented in the next section. The examination of the results follow and are presented in three sections: 850 nm, 850 and 780 nm, and lastly 780 nm. A summary and conclusion close out this report.

2. Experimental

The nanocomposite materials discussed in this report were produced by either air firing[2] or hot pressing, as previously documented by Fleischman et al.[1] A discussion on the optical microscope as well as the observation protocol is also included.

2.1 Materials Chosen for Analysis

Two different densification methods were employed to create specimens for analysis (Table 1). Pressureless, air-fire sintering was first explored to isolate the ideal ratio of MgO to Er:Y_2O_3. The ratio of Er:Y_2O_3 to MgO was varied around an average of 10 wt% (2.5, 5, 10, and 15). This represents a compromise between having sufficiently little Er:Y_2O_3 to inhibit its grain growth and limit optical scattering and having enough to provide adequate volume-averaged Er concentration for eventual lasing.

The second method of densification was hot uniaxial pressing under vacuum atmosphere. An Oxy-Gon Industries refractory-metal, miniature hot press, was used to sinter many of the materials discussed in this report. Further, the hot press was equipped with a linear variable differential transformer (LVDT) to track uniaxial shrinkage during the operation. A graphite die with a 1-inch inner diameter was coated with boron nitride (BN) spray and dried prior to use. The calcined powders were loaded in between BN spacers to prevent carbon contamination from the die at high temperature. A vibration table was used to assist with powder distribution in the die as well as to maximize the amount of powder loaded into the die.

Table 1 List of specimens, their corresponding chemical compositions (including weight percent [wt%]), and the imaging methods used

Specimen ID	Chemical composition	Densification procedure	Imaged by wavelengths	Specimen thickness
4CC29-3	Er:MgO		780 nm	
3CC151A	Nd:MgO		850 nm	3.70 mm
1VB113-400	90 wt% MgO, 10 wt% Er:Y_2O_3 calcined at 400 °C	Hot pressed at 1000 °C for 1 h, 25 °C/min heating rate.	780 nm	
1VB124-800	95 wt% MgO, 5 wt% Er:Y_2O_3 calcined at 800 °C	Air fired, 1400 °C hold for 1 h, 10 °C/min heating rate.	780 nm, 850 nm	…
2VB014	85 wt% MgO, 15 wt% Er:Y_2O_3 calcined 1200 °C	Air fired 1550 °C for 1 h, 10 °C/min heating rate.	850 nm	0.77 mm
2VB016	95 wt% MgO, 5wt% Er:Y_2O_3 calcined 1200 °C	Air fired 1550 °C for 1 h, 10 °C/min heating rate.	850 nm	1.83 mm
2VB018	90 wt% MgO, 10 wt% Er:Y_2O_3 calcined 1200 °C	Air fired 1550 °C for 1 h, 10 °C/min heating rate.	850 nm	1.79 mm
2VB062	96.5 wt% MgO, 3 wt% Er:Y_2O_3 calcined 700 °C	BN spray and spacers used in graphite die; 25 °C/min up to 1200 °C, hold for 10 min.	780 nm, 850 nm	…
2VB063[a,b]	96.5 wt% MgO, 3 wt% Er:Y_2O_3 calcined 1000°C	BN spray and spacers used in graphite die; 25 °C/min up to 1200 °C, hold for 10 min.	780 nm, 850 nm	1.14 mm
2VB059[c]	96.5 wt% MgO, 3 wt% Er:Y_2O_3 calcined 700°C	BN spray and spacers used in graphite die; 25 °C/min up to 1200 °C, hold for 30 min.	780 nm	…
2VB133	97.5 wt% MgO, 2.5 wt% Er:Y_2O_3	BN spray and spacers used in graphite die; 25 °C/min up to 1200 °C, hold for 30 min.	…	2.07 mm

[a] Used for the optical microscopy work.
[b] A smaller unpolished wedge not examined using the Z2m.
[c] A small pie-shaped fragment large enough for the Z2m but too small for the micrometer.

2.2 Optical Instrumentation

A Zeiss Z2m compound-optical microscope using AxioVision 4.9 software was used. The Zeiss Z2-M's hardware and software were configured to support subsurface grain studies of transparent/translucent ceramics. The critical element in permitting the NIR studies performed was the high-resolution monochrome (HRm) camera's nominal response curve out to 1000 nm (Fig. 3) and the built-in NIR signal-boost capability. This indicated a good potential for supporting in-line through transmittance studies using a monochromatic NIR LED source.

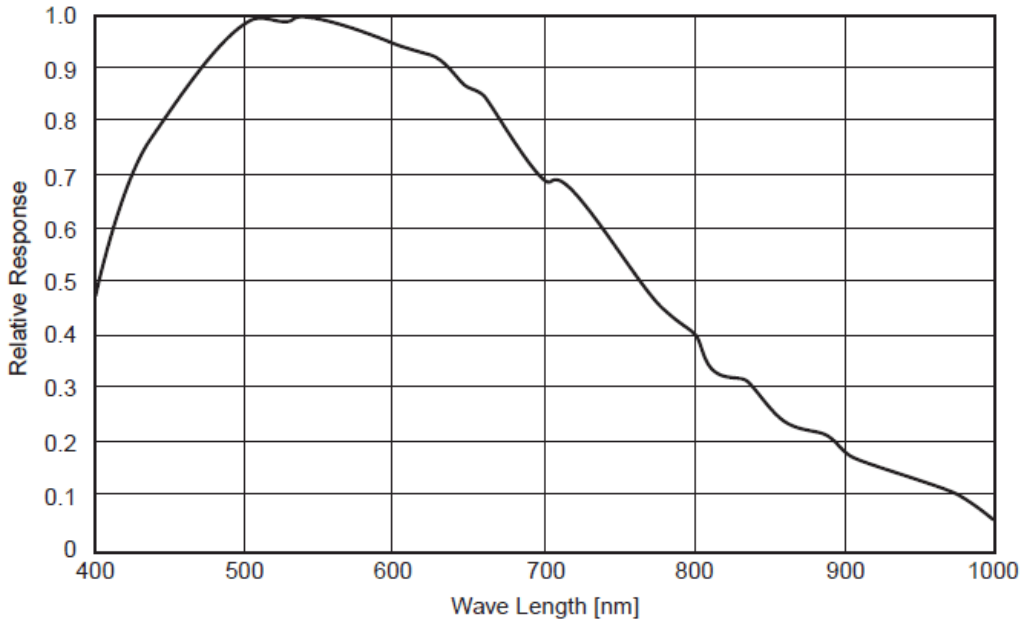

Fig. 3 Nominal response curve for the Zeiss HRm camera (used with permission of Carl Zeiss Microscopy)[3]

The hardware consists of the camera with NIR boost; a Zeiss HRm having a resolution of 1388 × 1040 pixels at 6.45 × 6.54 μm using a 1.00× projection lens. Multiple illumination methods were used: white LEDs, 5500 K, dedicated one transmission and one reflected; monochromatic NIR LEDs: 780 nm and 850 nm. A 940-nm LED also exists but was not used in this study. Multiple contrasting modes were also used: transmitted light for both white and NIR; reflected white light for bright field (RBF), dark field (RDF), and reflected polarized. Table 2 lists the properties of the Zeiss Z2m compound-optical microscope's objectives.

Table 2 Properties of Zeiss Z2m objectives

Objective/ numeric aperture (NA)	µm/pixel: HRm camera	µm/slice: AxioVision	Nominal field of view: 1388 pixels × 1040 pixels in µm
02.5×/ 0.06	2.58	102	3581 × 2683
05×/ 0.13	1.29	22	1791 × 1342
10×/ 0.25	0.65	5.9	902 × 676
20×/ 0.50	0.32	1.47	444 × 333
50×/ 0.80	0.13	0.41	180 × 135
100×/ 0.90	0.06	0.41	83 × 62

Optical resolution of an objective is dependent upon the wavelength being used, λ, and the lens's numeric aperture (NA), shown in Eq. 1. The Zeiss 20× and 100× objectives results are shown in Table 3. Resolution can be defined as being able to make precise repeat measurements, or to distinguish between two closely spaced features. Optical resolution is partially wavelength dependent as shown by Eq. 1. Not all optically observable features are resolvable, regardless of the objective chosen.

$$\text{Rayleigh resolution (r)} = 0.61\lambda/\text{NA} \quad (1)$$

Table 3 Comparative Rayleigh resolution based on wavelength

Objective	Wavelength (ʎ)	Rayleigh resolution (r)
20X/NA 0.5	0.550 µm[a]	0.61 µm
20X/NA 0.5	0.780 µm	0.95 µm
20X/NA 0.5	0.850 µm	1.04 µm
100X/NA 0.9	0.550 µm	0.37 µm
100x/NA 0.9	0.780 µm	0.529 µm
100X/NA 0.9	0.850 µm	0.576 µm

[a] 0.550 µm is the commonly used wavelength to define the color green, which is the highest-response color of the human eye and most common sensor chips.

Table 4 lists the total beam power of each of the NIR LEDs for general comparative information.

Table 4 NIR LEDs (used with permission of Thorlabs)[4]

Item no.	Color	Housing	Total beam power[a]
M780L3-C4	IR	[redacted]	180 mW
M850L3-C4	IR	[redacted]	400 mW
M940L3-C4	IR	[redacted]	380 mW

[a] At center wavelength

Figures 4–6 are normalized curves for each particular spectrum, which is important when discussing Er luminescence properties. On-site instrumentation did not exist to accurately measure the actual spectra and the analog power controller is incapable of making the required repeat settings accurately. No comparable spectrum could be found for the Zeiss white-light 5500K LEDs. Also not found are any intensity verses applied power data.

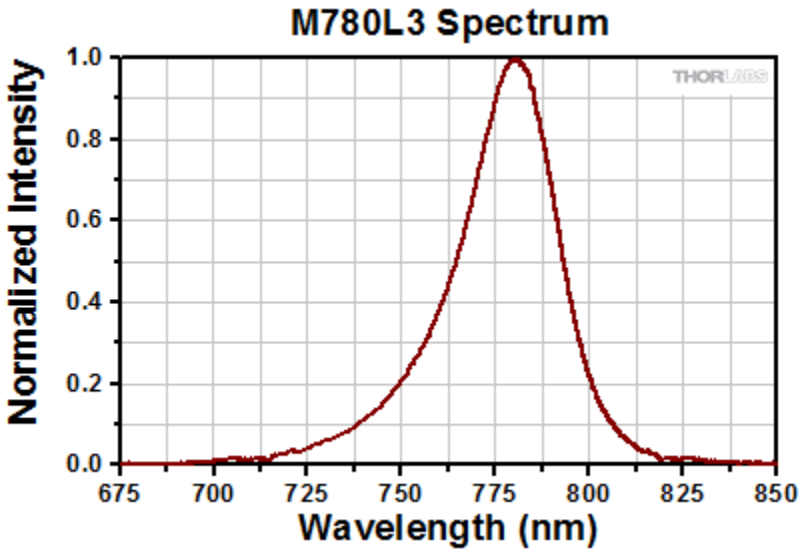

Fig. 4 Normalized curve for M780L3 spectrum (used with permission of Thorlabs)[4]

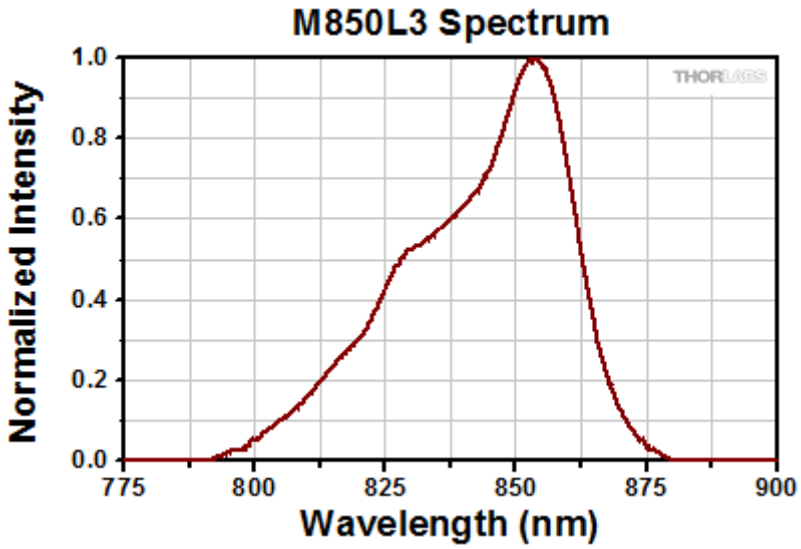

Fig. 5 Normalized curve for M850L3 spectrum (used with permission of Thorlabs)[4]

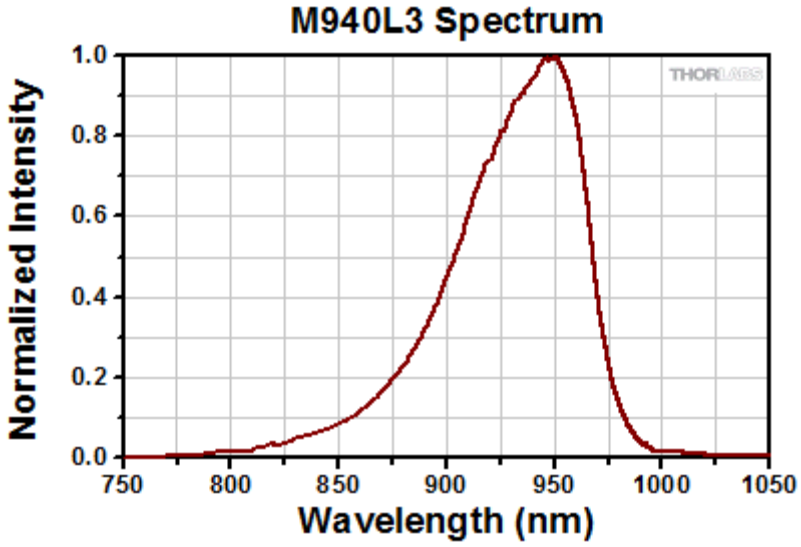

Fig. 6 Normalized curve for M940L3 spectrum (used with permission of Thorlabs)[4]

Figure 7 shows the back of the Z2M stand with the top unit for reflected light and the bottom unit for transmitted light. The white and monochrome LED lamps (the system's illumination capability) are on the left and right side, respectively, of each unit. Figure 8 shows the Z2m "light paths" for the reflected and transmitted light and "optical paths" for the monochrome and color cameras. (More information on the Z2m can be found in an ARL technical note published in 2019.[5])

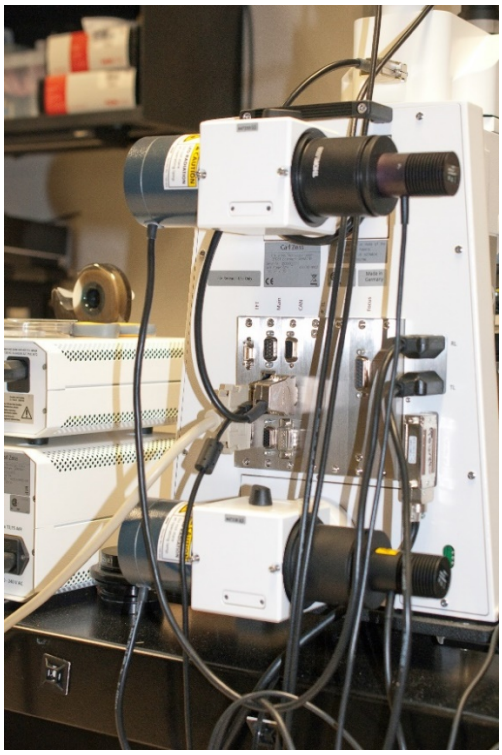

Fig. 7 Back of Z2m stand showing reflected light module (top), transmitted light module (bottom) with white LEDs (left side, each module), and monochrome LEDs (right side, each module)

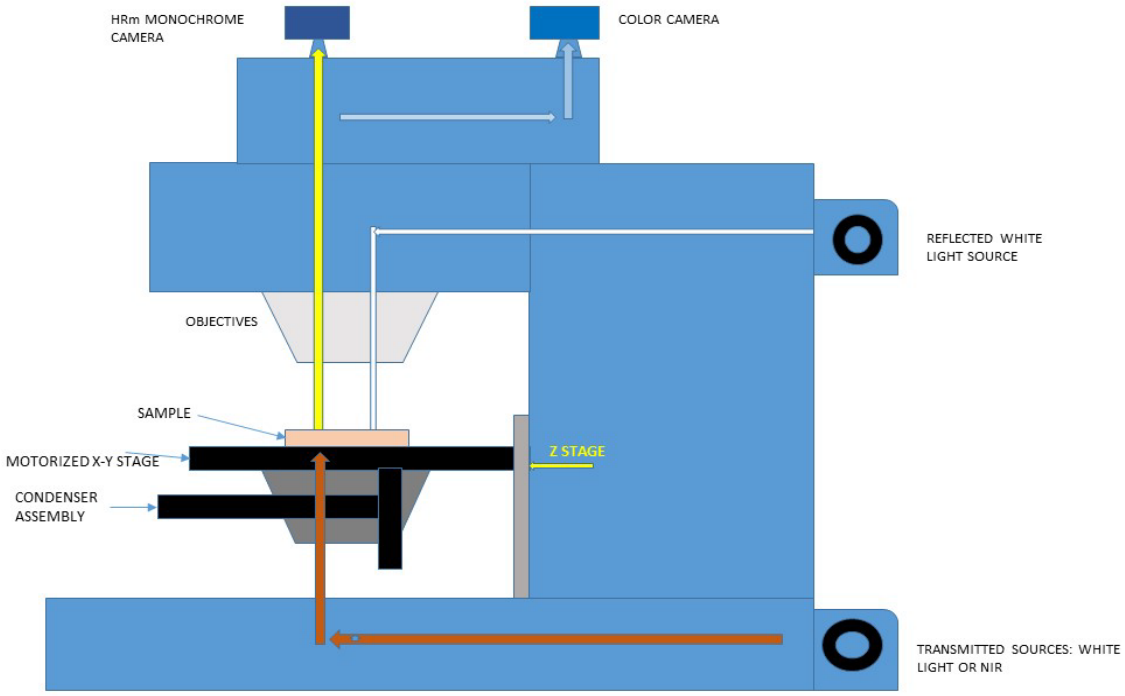

Fig. 8 Light paths, white and brown, and the objective to camera optical paths, yellow and light blue

The Z2m condenser is an achromatic-aplanatic design possessing two lens assemblies consisting of seven lenses total between them, with one assembly able to be removed from or employed into the transmitted beam path. The unit supports transmitted brightfield, darkfield, phase, and differential interference contrast modes. It has its own aperture using objective NA values for settings. The unit is not automated.

The software is the 64-bit version of AxioVision 4.9. The base program controls the stand, stages, and camera functions. Manual input is required for all usage, as there is no macro capability. Only two application modules were used: multidimensional 3-D and extended focus. The 3-D module is used to define the Z-stack (a series of individual images taken along the Z-axis) limits and to determine the optimal slice spacing based on the objective employed. The extended-focus module fuses individual Z-stack slices into a single-frame image possessing a greater depth of field than the individual slices. The wavelet algorithm option within the extended-focus module, for which no description could be found, was used for all image-fusion processing.

2.3 Microscope Observation Protocol

Specimens were mounted over an appropriate-sized aperture on the stage. Most specimens required the use of a metric drill gauge, as they were too small to fit over the standard stage insert aperture. For partially polished specimens, the polished face became Face 1. Reflected white light (RBF) helped align the specimen and establish the initial focal point. Transmitted white light (TBF) was required to assure no edge illuminations and a minimum of off-axis stray-light generation. An RBF survey of the top face was performed prior to the in-line transmitted NIR evaluation. Camera and lighting adjustments were performed as required. The process was then repeated on Face 2. On several occasions, RDF was required to help elucidate what was being observed.

3. 850-nm Imaging Results

Initially, three specimens were examined using white light in an RBF mode and the 850-nm source using TBF mode. White-light RDF mode was also use for some specimens. These specimens are all Er:Y_2O_3–MgO compositions—2VB014, 2VB016, and 2VB018—as documented in Table 1. No two specimens imaged the same, likely caused by variations in processing, composition, grain orientations, and/or aggregations. At times differences in apparent optical properties were observed at different points of the same specimen.

3.1 Specimen 2VB014

The compositional information provided in Table 1 for 2VB014 is 15 wt% Er:Y_2O_3 and 85 wt% MgO. Figure 9 consists of a back-lit macroimage at 1× with several features that are not easily categorized (i.e., near face, far face, and subsurface). A Nikon DSLR camera with a 105-mm macrolens using a 5000-K light board was used to capture the back-lit image in raw format. The raw image's brightness and contrast can be manipulated to emphasize some near face features, allowing assessments of the number of features present, apparent size, distribution, and general location. Adobe Light Room was used to process the captured images and then export them as JPGs. Unfortunately, the features of interest appear to be NIR transparent at 850 nm and the specimen fluoresced, so only minimal information could be extracted from any image.

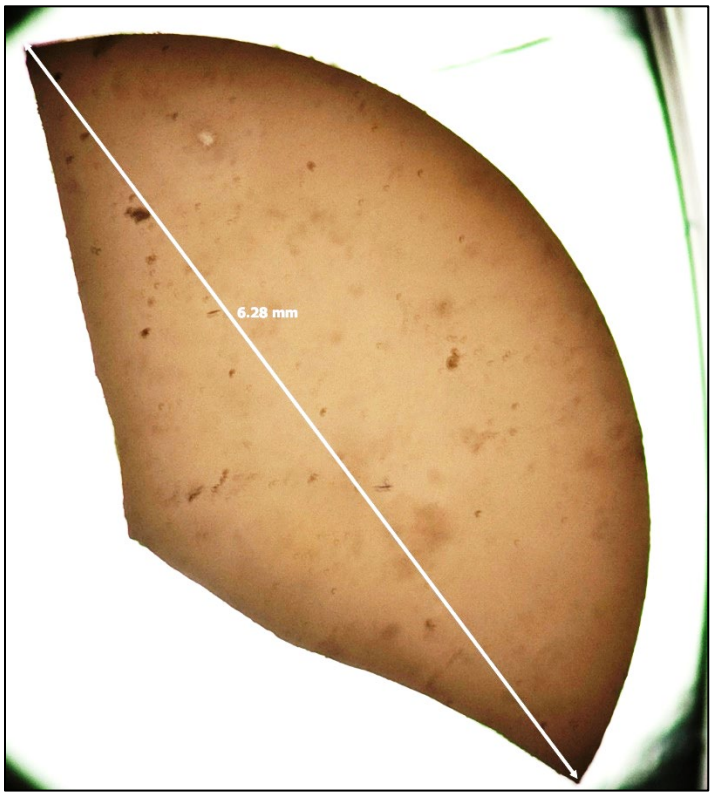

Fig. 9 1× macro backlit image of 2VB014 made using a light box with DSLR and 105-mm macro lens

RBF imaging of 2VB014 revealed a surface appearing to be unpolished with a rough surface on Face 1 at 10× (Fig. 10) due to the crowded speckled black–white contrast. The reason for the large black areas in the image could not be determined optically. The easiest explanation is they are agglomerates of the smaller black particles.

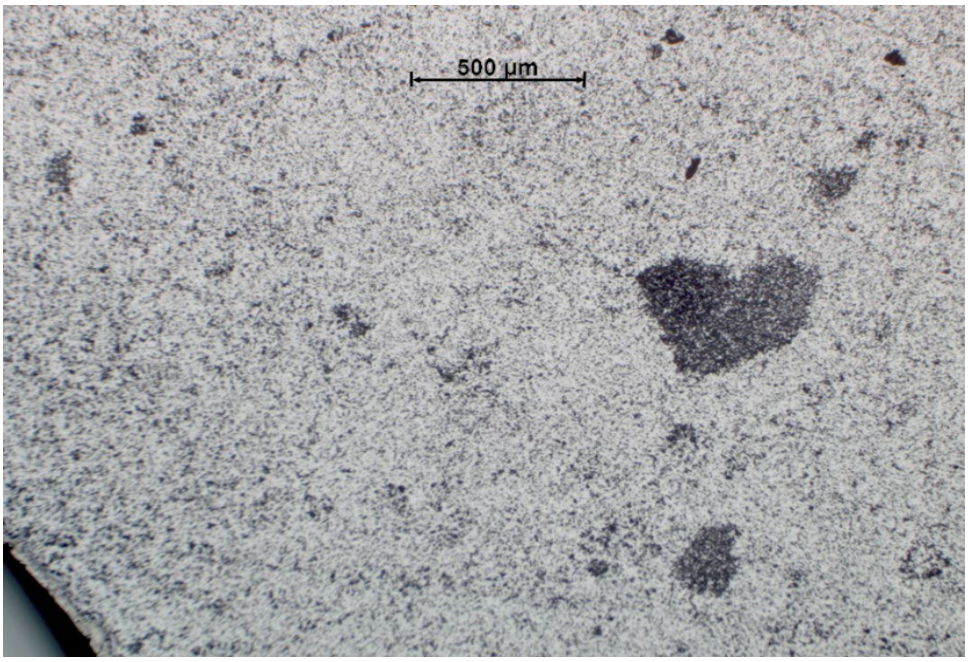

Fig. 10 RBF grayscale image of the polished face of 2VB014, Face 1 at 10×

In Fig. 11, a TBF image using 850 nm, at 20× the Face 1 surface appears partially polished and smooth. Many of the darker features from Fig. 10 are largely absent and replaced by mid-tone gray areas in Fig. 11, smoothing the surface appearance to the eye; note the cluster on the right but otherwise the dark features are largely well dispersed in most of the frame. The arrows highlight those fine white spots in the light-gray matrix that do not show up well in this size format but are readily visible in a full-frame monitor display. The bright spot, as indicated by the yellow arrow, may be an aperture-adjustment issue or the result of aperture–nanocomposite interaction; its appearance is random.

A few nanocomposite specimens appeared to act like another optical element in the optical train. These optical anomalies were observed across the whole specimen or were isolated in specific specimen sections. Related anomalies occurred while performing subsurface-grain-boundary studies on 3- to 6-mm-thick magnesium aluminate spinel ($MgAl_2O_4$). A reflection of the stage plate appeared approximately 1.2 mm deep in the specimen only to fade at a depth of 1.4–1.8 mm. In an earlier ARL report,[6] the specimen grains were visible outside that foggy reflective layer (in Figs. 23 and 24). It was found there existed a midsection of smaller, tighter grains.

The white arrows of Fig. 11 point to white dots that are presumed to be yttria, as yttria is the minor constituent or phase in the 2VB014 nanocomposite at 15 wt%. At 20× the dots are visible in a full-scale monitor image, but not resolvable. The

medium-gray area is likely also a luminescence result but more uniform in appearance as a result of internal random scattering. The bright area on the left-hand side (yellow arrow) of the image was believed to be due to light scattering by the Er fluorescence. Erbium-fluorescence emanation tests were performed as seen in Figs. 12 and 13. The remaining light/dark patterning is likely surface features.

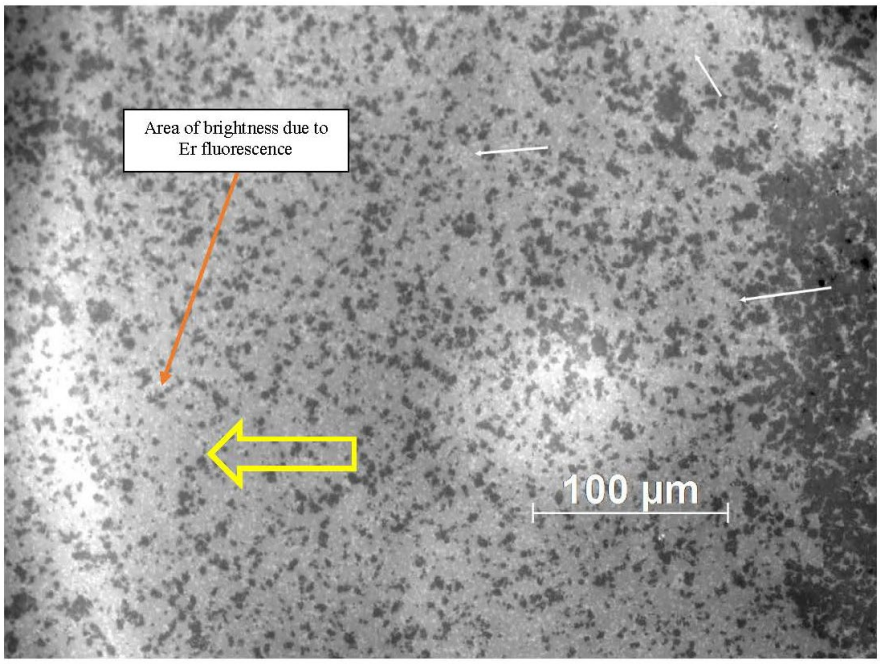

Fig. 11 20× 850-nm TBF image of 2VB014's polished surface appears less rough; note two bright areas and the white dots at the arrows, Face 1

Figures 12 and 13 depict a fluorescence emanation test. The color camera will only respond over the 400- to 700-nm range, sometimes referred to as the visible spectral range. Physically, the camera's sensor is covered by a 700-nm cutoff filter, rendering the color camera NIR blind and incapable of responding to the 850-nm beam. In both Figs. 12 and 13, the fluorescence emanation test showed the specimen's bottom surface was illuminated at 850 nm while the top surface was clearly visible to the color camera. The Er in the nanocomposite body was activated by the 850-nm NIR light; the visible top surface demonstrated fluorescence and was captured by the color camera. No white-balance corrections were made for either figure.

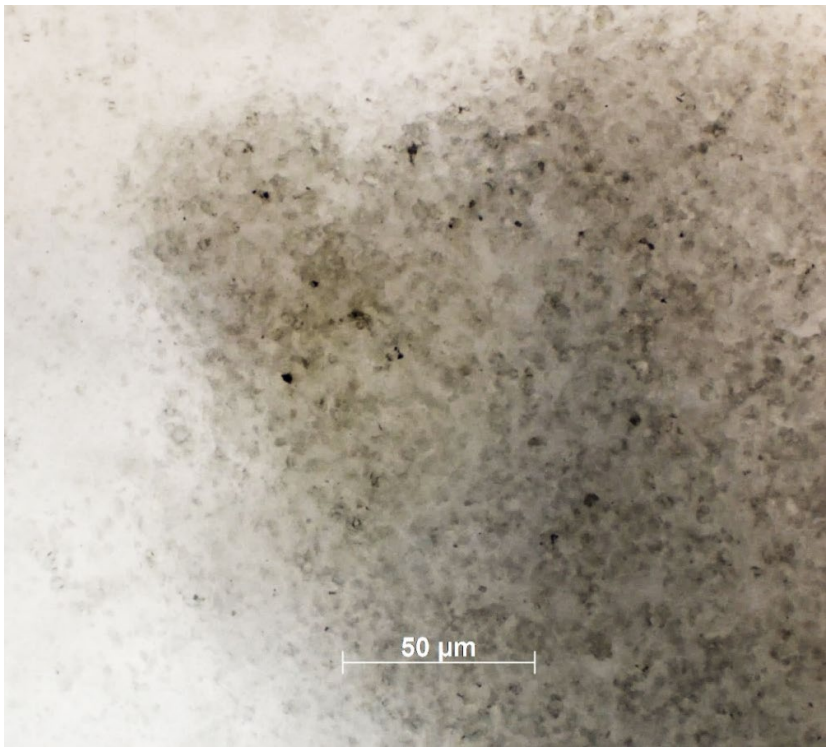

Fig. 12 Color camera at 50× using 850-nm TBF illumination, polished Face 1, 2VB014

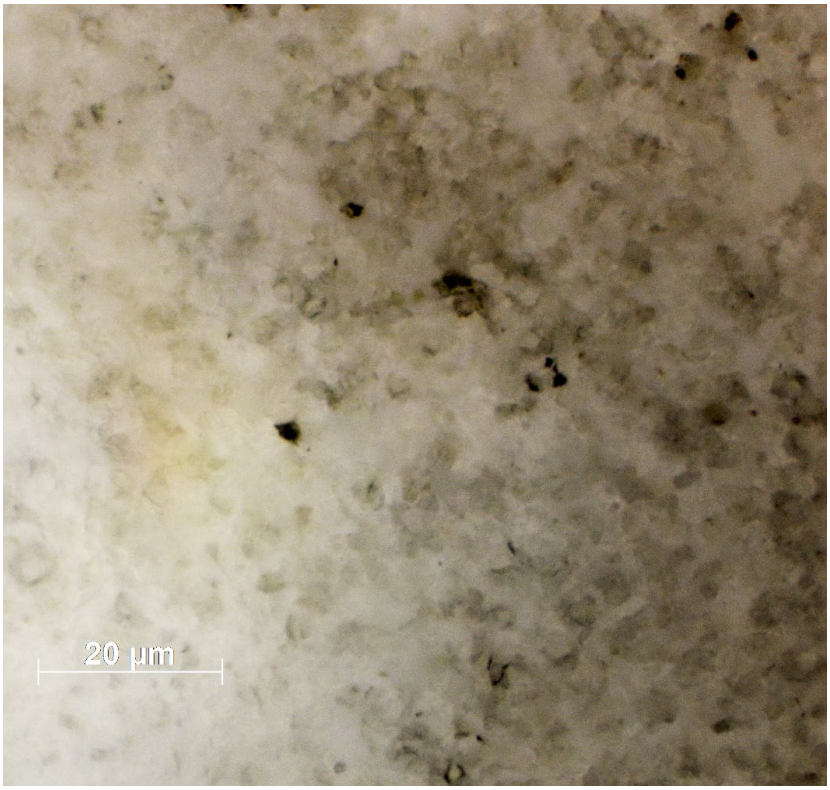

Fig. 13 Color image at 100× of 2VB014 polished face using TBF 850-nm NIR illumination

An uncorrected color RDF image using LED white light (Fig. 14) at 5× yields an entirely different perspective for this surface, revealing an aggregate capable of causing the localized variations seen in Fig. 11. The reverse unpolished Face 2 was not analyzed, given the difficulty encountered with Face 1 and the fluorescence issue. The effort at this point was still subsurface investigation for the presence NIR through transmission interferents.

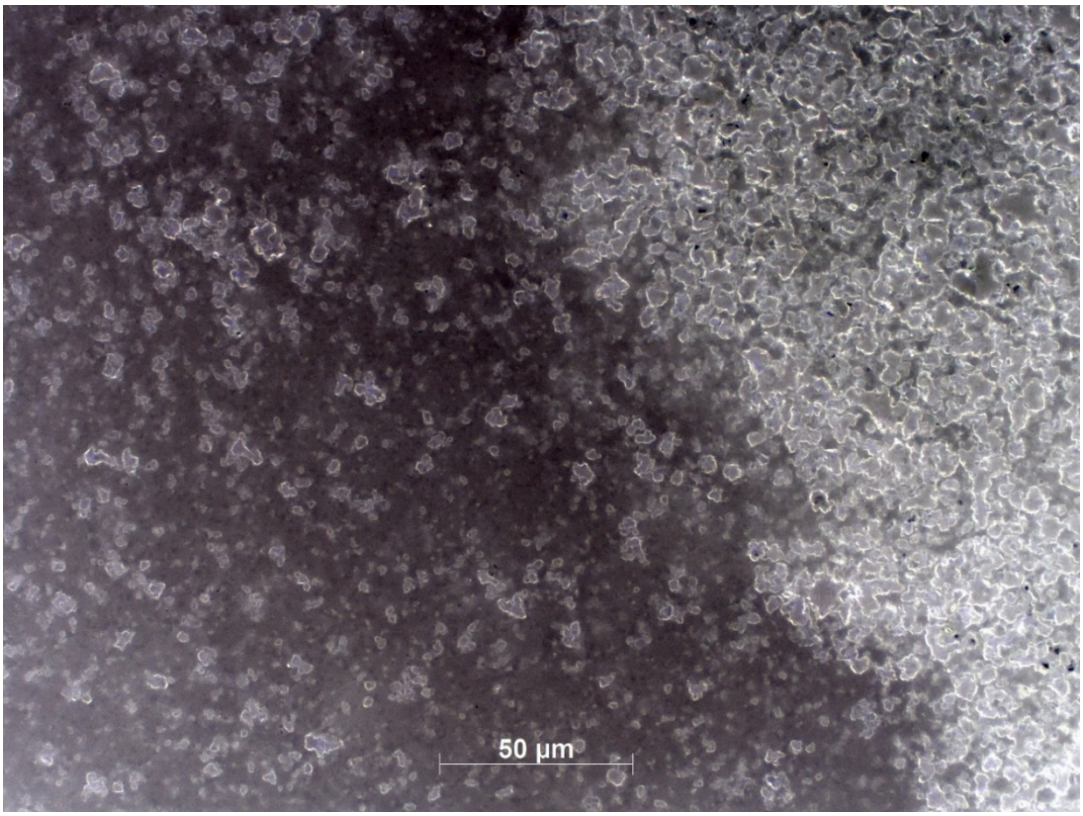

Fig. 14 Uncorrected color 5× RDF image of the polished Face 1; note the highly transparent agglomeration on the right, 2VB014

3.2 Specimen 2VB016

The given composition of 2VB016 from Table 1 is 95 wt% MgO and 5 wt% Er:Y_2O_3 and was air-fired. Figure 15 shows polished Face 1 of the specimen as imaged using the Nikon color camera at 1× magnification. The brightness of the image has been adjusted to see apparent inclusions as indicated by the yellow arrows.

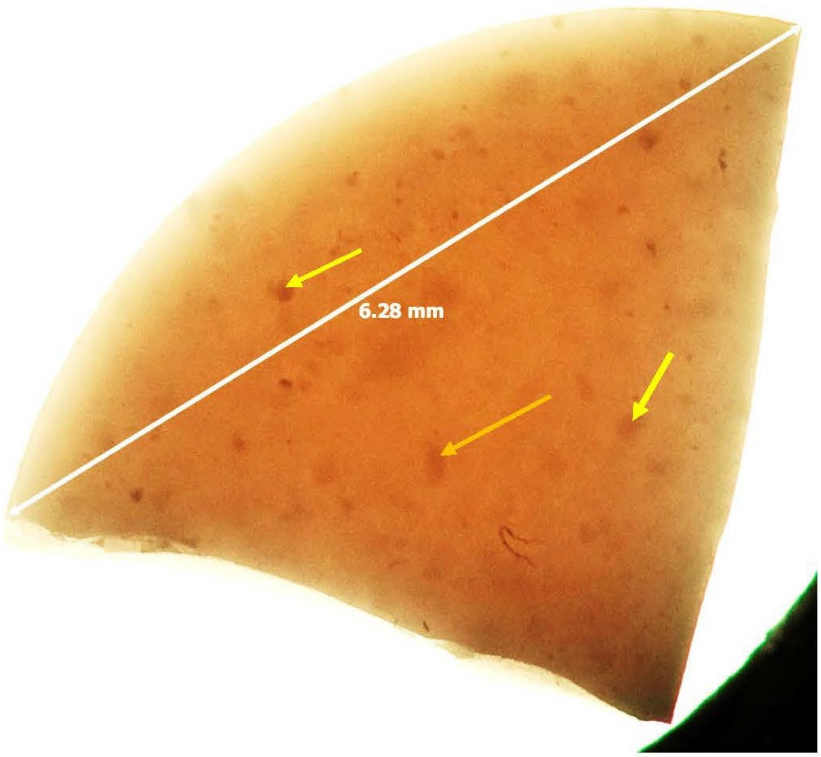

Fig. 15 Uncorrected color macroimage of 2VB016 with brightness adjusted to see apparent inclusions

Using RBF lighting, the polished Face 1 in Fig. 16 appears contaminated and/or marred, likely due to incomplete polishing of the specimen surface. The double-headed black arrows indicate probable polishing direction. The single-headed arrow indicates a feature apparently disrupting or overlaying the polishing scratches, likely debris from the storage bag. The striking change in appearance between Figs. 15 and 16 arises from the 1) specular reflectance by the nanocomposite surface of the RBF light enhancing the visibility of any surface defect and 2) switch from color to grayscale images.

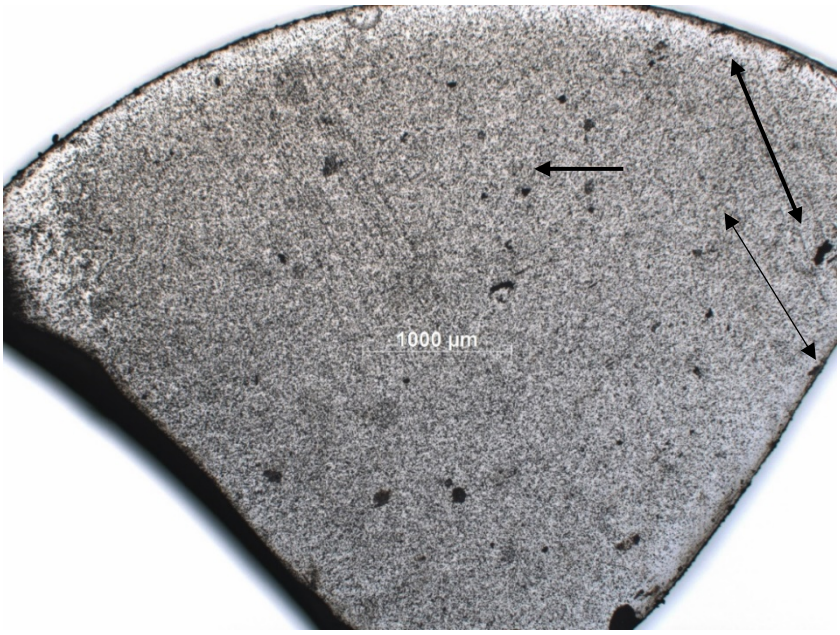

Fig. 16 Grayscale image of Specimen 2VB016 at 2.5× using RBF lighting

Figure 17, a 50× image, exhibits four different morphologies with three distinct reflectance bands. The A and B arrows indicate two apparently different-sized morphologies with A indicating a slightly larger morphology than B. It is also possible the grain orientations are different rather than size. Figure 18 is a 4000× secondary scanning electron microscope (SEM) image, which is every bit as confusing as its 50× optical version. The green hue in Fig. 17 is the result of the AxioVision software exporting the grayscale image as a 24-bit color JPG, which is the default setting. Both the optical image and the SEM image, Figs. 17 and 18, respectively, demonstrate the complexity of 2VB016 physical structure.

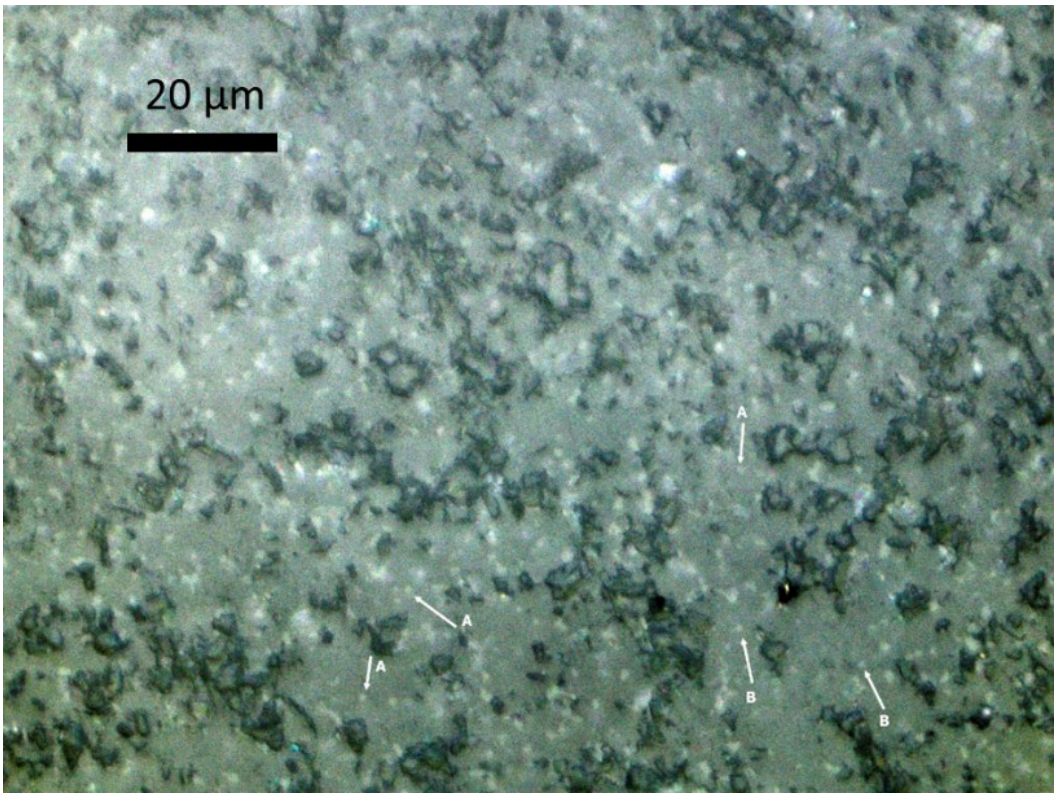

Fig. 17 In 50× image of 2VB016, note four distinct morphologies and three tonal values; white arrows point to white specks of two sizes

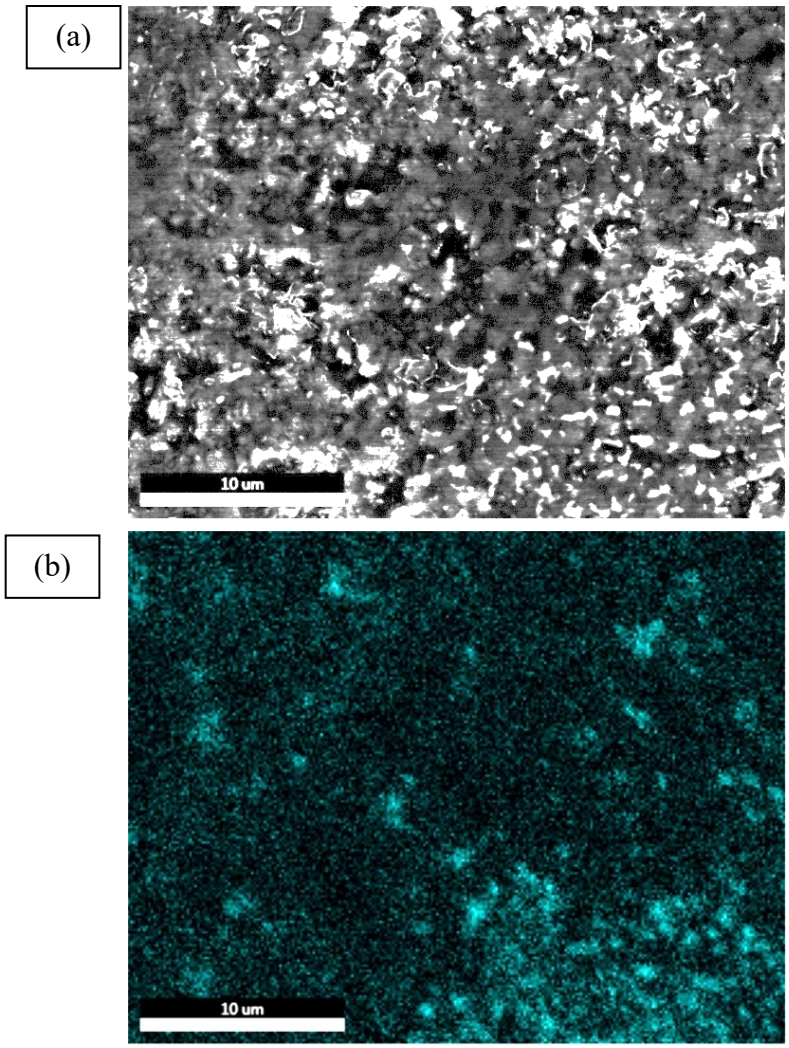

Fig. 18 a) 4000× Face 1's SEM micrograph of 2VB016 and b) energy dispersive X-ray (EDX) yttrium map of image captured at 4000×

Despite the carbon coating, in Fig. 18a there is enough charging to render the image less clear than Fig. 17. The EDX map of yttrium distribution in Fig. 18b appears to indicate the presence of medium-sized yttria inclusions clustering at lower right. The map was collected using a 256- × 200-pixel frame for a 2048- × 1600-sized micrograph at 50 μs per frame for a minimum of 200 frames. The pixelated appearance is a result of collection frame size. The faint clustering nodes may indicate more yttria is present than indicated by the SEM micrograph or be the result of beam drift during mapping. Particle orientation and partial burial by the MgO may also account for these apparent discrepancies. The EDX elemental spectrum in Fig. 19 reveals a simple four-element specimen underlying the physically complex-appearing material. The carbon peak at far left was not automatically identified due to poor baseline correction.

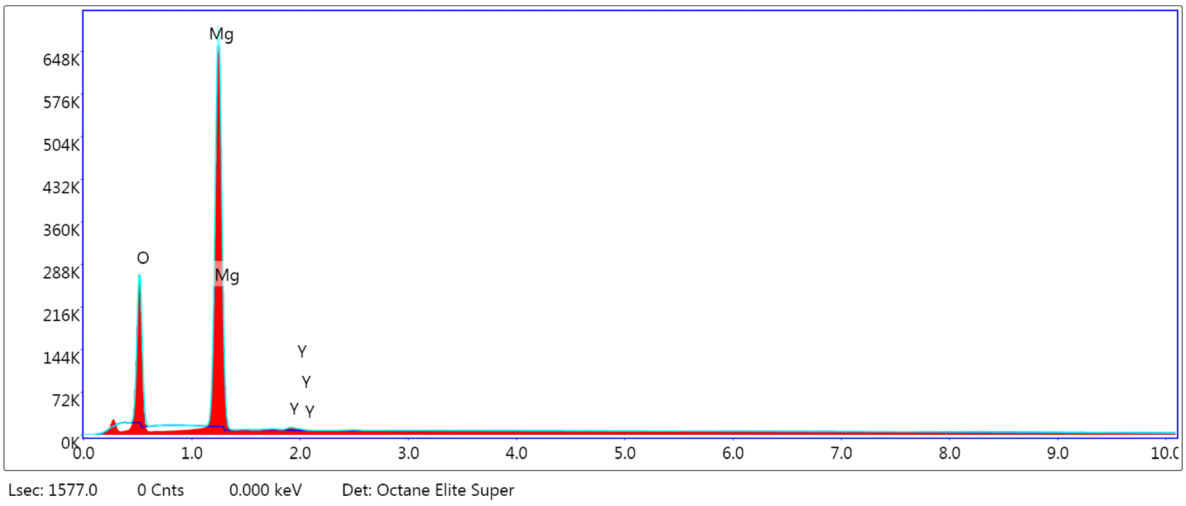

Fig. 19 EDX spectra of the area imaged in Fig. 18 missing any indication of erbium peaks

Figure 20, with 50× capture field dimensions of 180 × 135 µm, shows surface-height variations possibly resulting from the grinding of this specimen. The two or three coronas, bright white flares, are a dark-field result arising from the oblique angle needed to create dark-field illumination and the incident beam diffracted by an edge.

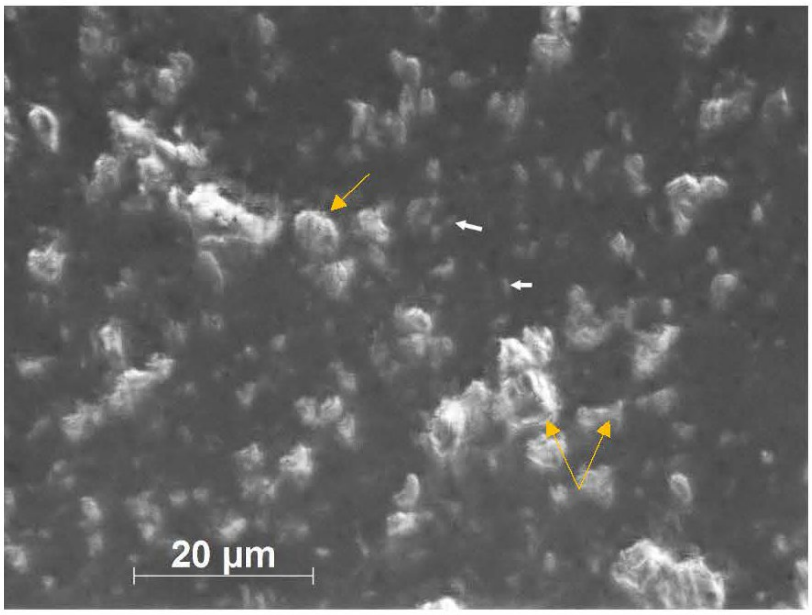

Fig. 20 50× 2VB016 RDF image with what could be a second phase at the white arrows; yellow arrows identify edge flaring, Face 1

Figure 21 is a 20- × 850-nm TBF image from Face 2, which exhibits numerous dark and light spots. It was suggested the dark spots could correspond to the brighter phase in the backscattered SEM image (Fig. 22). Unfortunately, at higher magnification, the entire surface became fuzzy and features at the arrows could not be resolved.

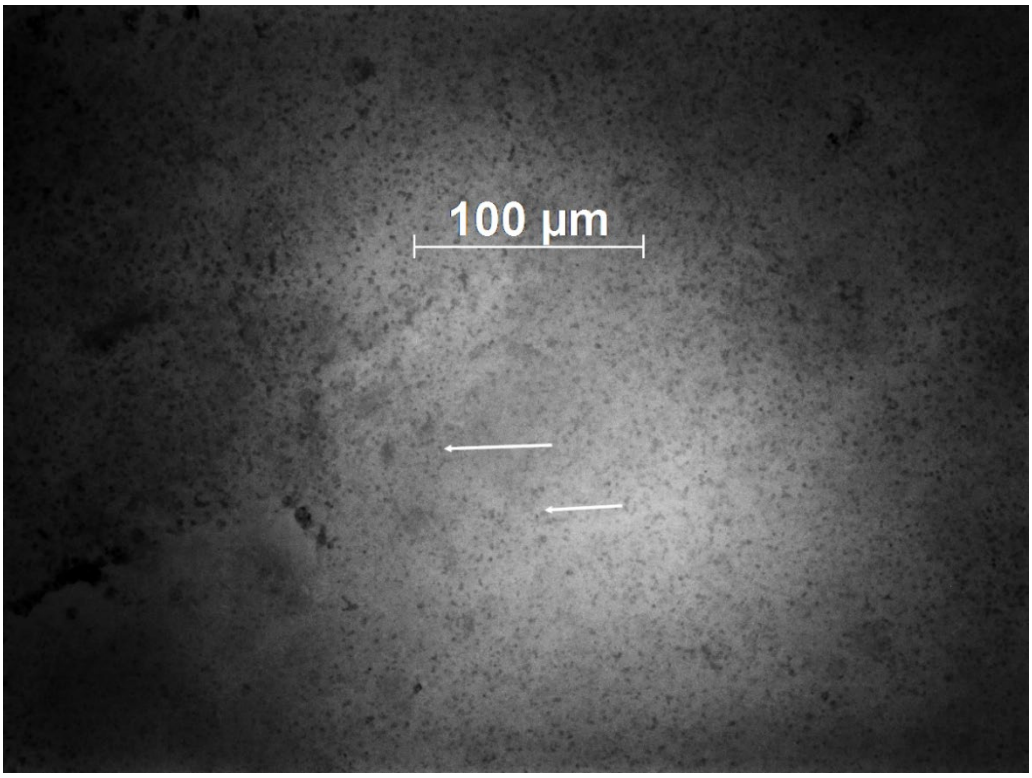

Fig. 21 Optical image of Face 2 of 2VB016, 20× using 850-nm TBF, showing the best resolution possible; arrows indicate features that normally could be resolved at higher magnifications

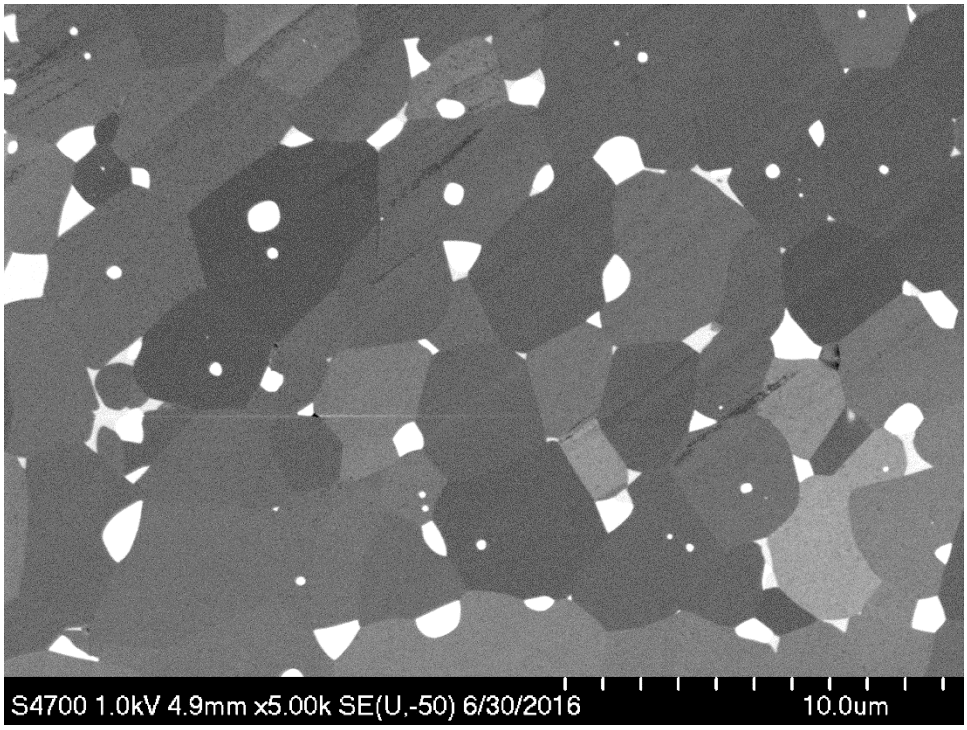

Fig. 22 Backscattered-electron SEM image of polished cross section of 2VB016 at 5000×

Figure 23 is a 20× transmitted 850-nm illuminated specimen. The 850-nm power source was modulated in an attempt to generate a usable image. Figures 12 and 13 of 2VB014 used full power; had full power been used here, the bright center spot of Fig. 23's Face 2 would appear as a glaring white, featureless ball and the gray areas thinned, rendering the image useless for analysis. The features seen are part of the processing surface skin of the unpolished Face 2.

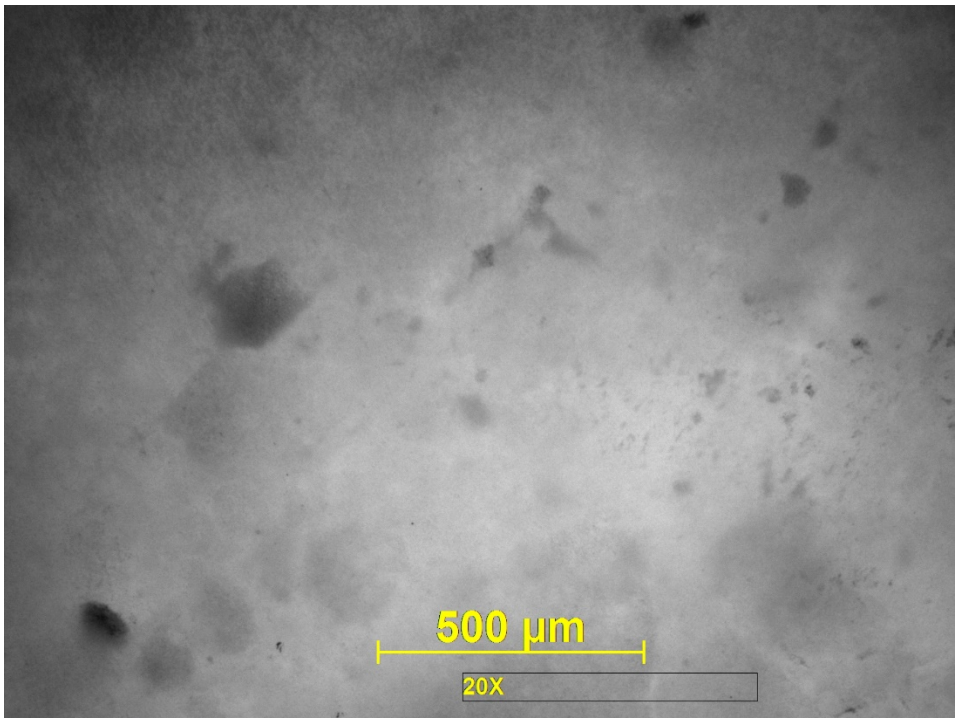

Fig. 23 Optical image of 2VB016 Face 2's response to moderate 850-nm NIR at 20× magnification

3.3 Specimen 2VB018

Specimen 2VB018 is an air-fired 90 wt% MgO with 10 wt% Er:Y_2O_3 specimen, shown as a 1× macro-image in Fig. 24. Using transmitted 850-nm light, the internally scattered Er glow effectively masked any subsurface features.

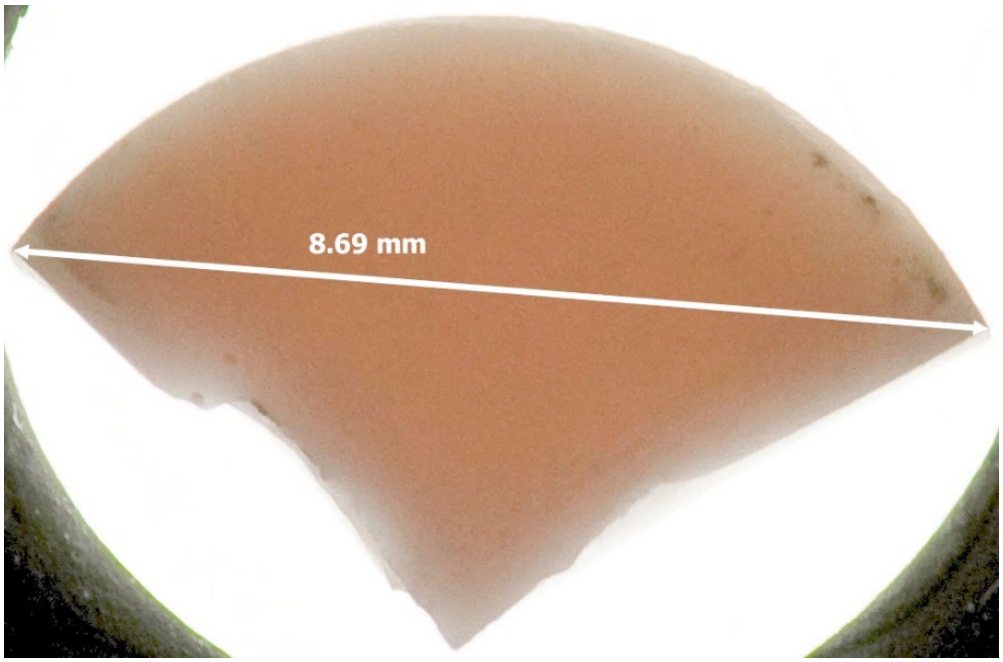

Fig. 24 Color macro-image of 2VB018 (1×); note the lack of obvious internal features

Figure 25 is a 50× RBF optical, single-frame image of 2VB018 with apparent ceramic protrusions as the result of the left side being out of focus. The white specks could not be resolved optically using any mode of available illumination. Notice the rounded nodes appearing to protrude above the general surface. The 50× magnification generally proved the upper limit of resolution for the AxioVision extended-focus algorithm for this type of middle-toned frame.

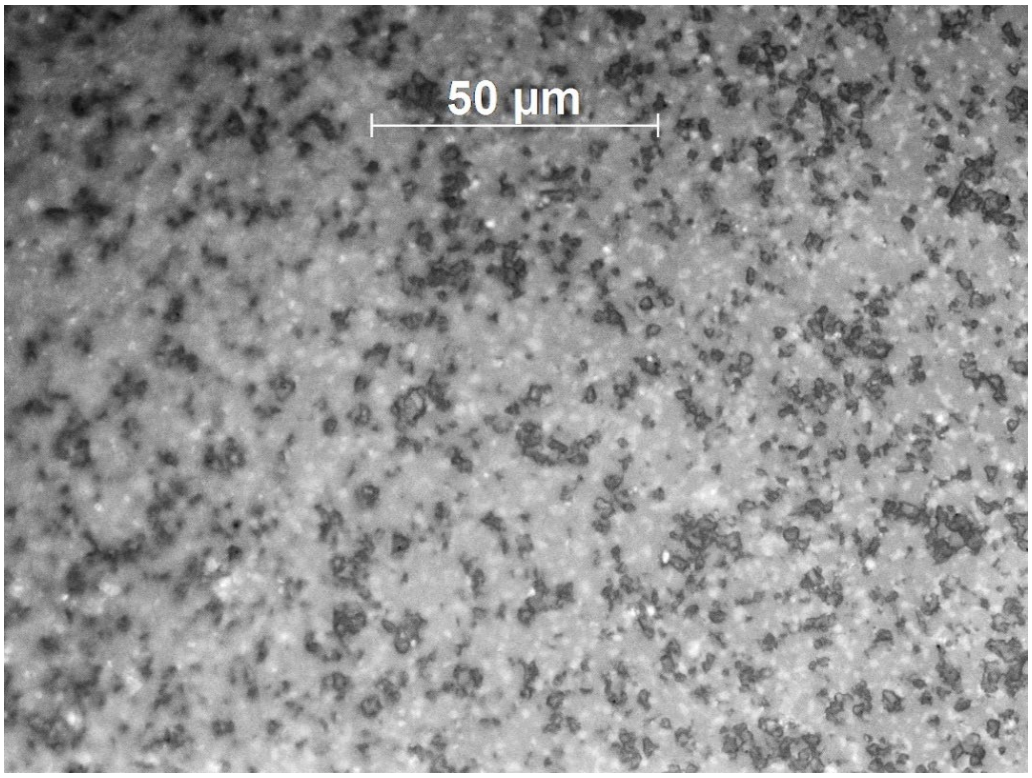

Fig. 25 50× RBF optical image of 2VB018 polished Face 1

Figure 26 is one of the few "in-focus" 100× images captured in this study. While the overall contrast limited the extended-focus module in generating a high-resolution image, an expanded number of surface features is evident. Though polished, there appears to be a micron-scale roughness present.

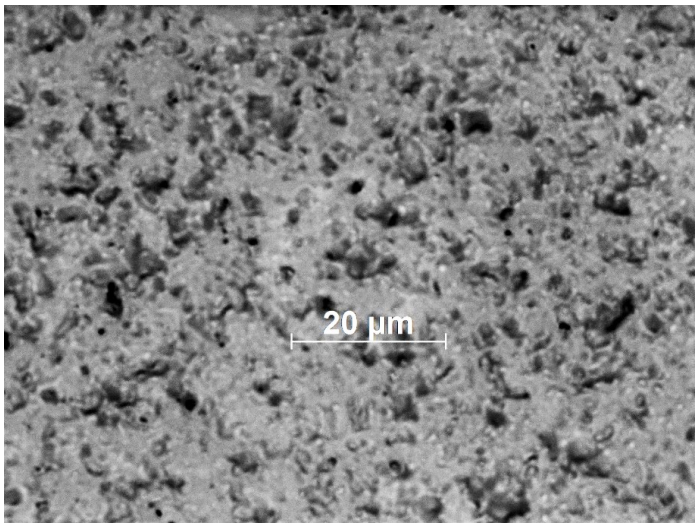

Fig. 26 100× RBF optical extended-focus image of 2VB018 Face 1

Figure 27 is a 100× RDF Face 1 extended focus with reduced sharpness arising from fuzzy Z-slices. That effect possibly originated from stray light interacting with the rough surface texture of the exposed ceramic; or, conversely, there was not sufficient contrast for the algorithm to work. The stack-processing algorithm has no adjustment features except to use an alternative fixed algorithm, which has proven to produce even worse final images.

For this and several other specimens, the use of RDF randomly provided additional information regarding near-surface aggregates not possible with bright field images. RDF imaging magnification of extended-focus images tends to be limited to 20× or 50× depending on the material and the microtopography. The degree of edge flaring is one common limitation, as are extreme topographic variations.

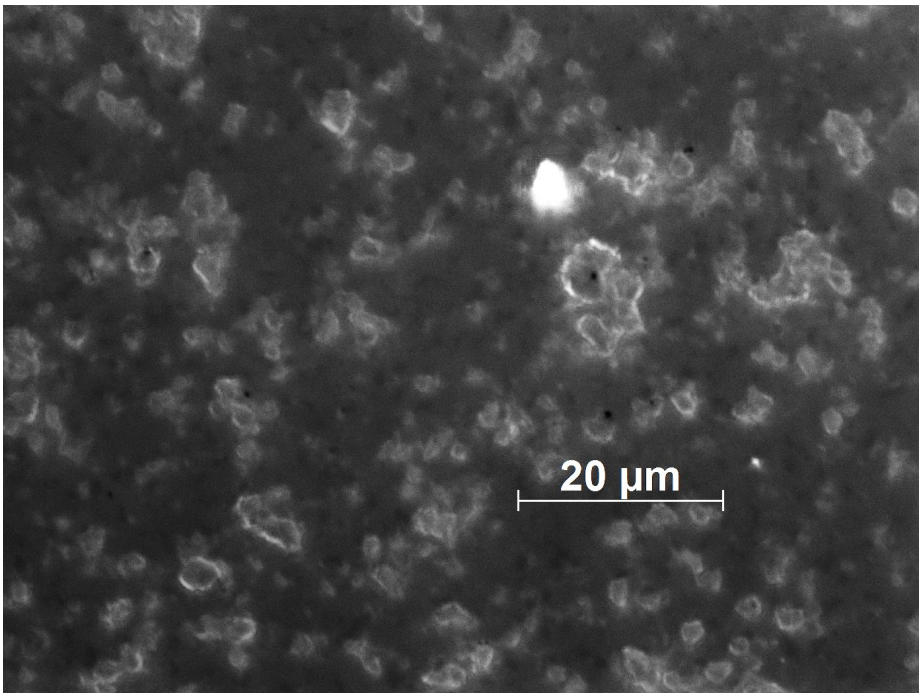

Fig. 27 100× RDF Face 1 optical image of 2VB018; blurry dark-field image caused partly by edge flaring common in high-magnification RDF images

Figure 28 illustrates the effects of microtopography waviness on image quality. Most of the image appears uniform with sharp edges; the light field seems to diminish left to right but not the crispness of the features. The use of transmitted light with 2VB018 only proved productive for one face and then only with white light. The 850-nm source was unable to adjust the light field to a usable level with this specimen.

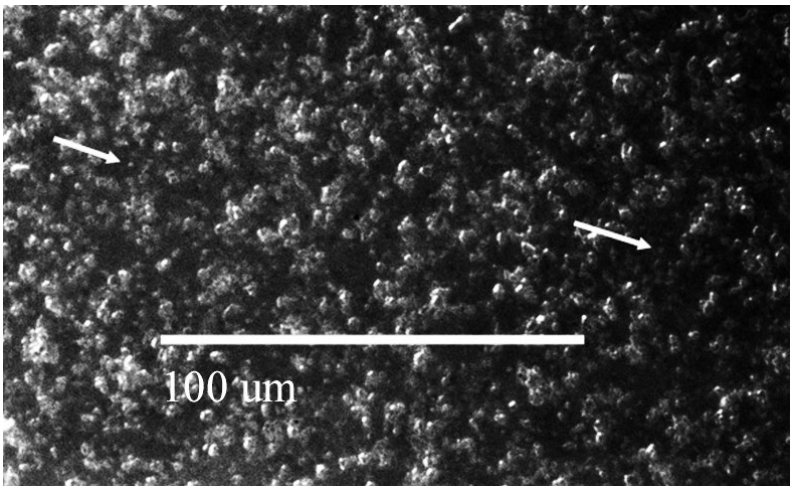

Fig. 28 50× RBF image of 2VB18 Face 1 illustrating effect of surface curvature, as indicated by the arrows

3.4 Typical Imaging Problems

While the three specimens discussed previously could be illuminated with some difficulty due to what was identified as Er luminescence, imaging problems with other specimens arose at 850 nm when the imaging parameters were unable to be sufficiently adjusted to produce usable images. Specimen 2VB063, a hot-pressed specimen (Table 1), was used as an example in this subsection. The distortions in the images shown in the remainder of this subsection were not limited to this specimen, having occurred in all transmitted 850-nm illuminated nanocomposite specimens. Micron markers and magnification data were not annotated for these unanalyzable images as the effort at this point was to test adjustments to generate usable micrographs.

Figure 29's two images are atypical for the majority of transmitted 850-nm imaging issues but support the contention for lens-like properties in some specimens. In Fig. 29, Photo A is as taken, with no postprocessing. Photo B was processed using MS Photos vignette tool, and demonstrates what are abnormal beam optics for Zeiss system lenses; a plane surface appears to possess a cylindrical shape. The yellow arrows in Fig. 29A indicate apparent necking or structuring, which persisted postprocess in Fig. 29B. Use of the lower-aperture lens in conjunction with the specimen's internal structure is the most likely source for this behavior. Figure 29 exhibits an actual flat surface area appearing to be tubular in structure. Normally, that type of behavior requires special-purpose optics.

Micron markers and magnification data were not annotated for these unanalyzable images as the effort at this point was to test adjustments in an effort to generate usable micrographs.

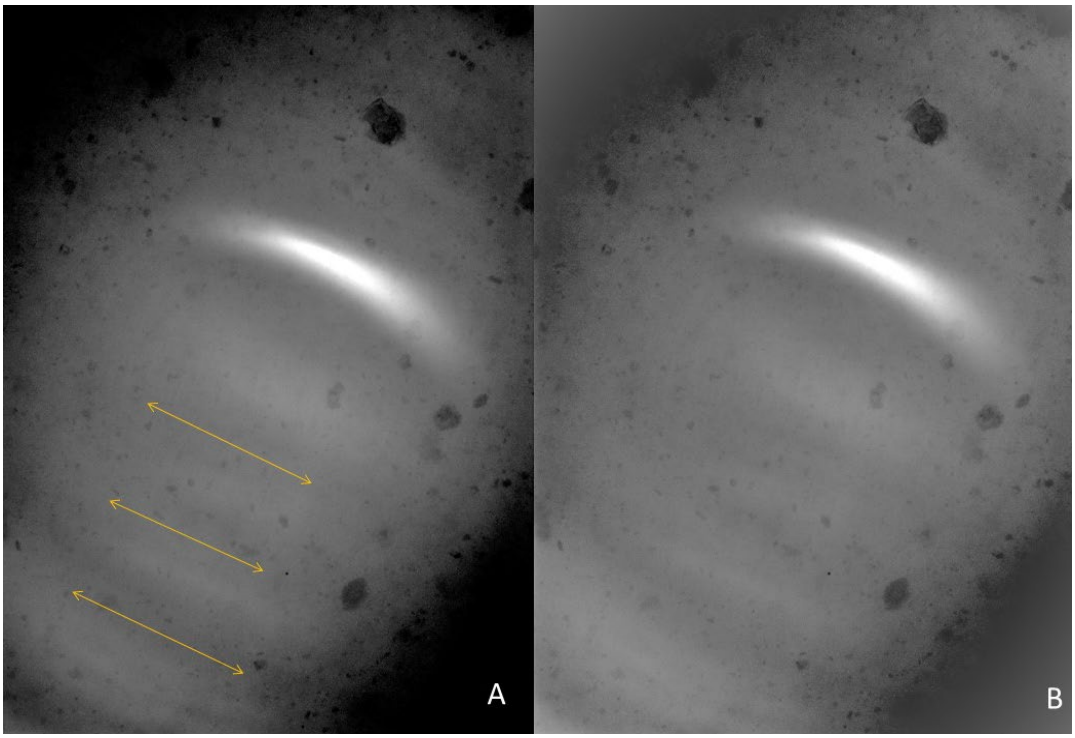

Fig. 29 Unanalyzable 2VB063 transmitted 850-nm image; left) yellow arrows mark the apparent surface stricturing, which persisted post-vignette correction processing

Figures 30 and 31 are more typical for unusable 850-nm images and no ready explanations are available for those effects. The visible-spectrum Er luminance cannot be the sole origin for this type of distortion, only a possible contributor. The 850-nm beam's interaction with the aperture lenses and the nanocomposites' internal structure are the most likely prime causes, which do not lend themselves to optical modeling due to the complexity of the system.

Figure 30 would be a vignette image if the oblong bright spot were not present. Image vignette can be defined as having a clear center and a uniform fading away towards the image edges. The oblong bright spot may arise from the condenser's bottom lens. This effect most often occurs when using reflected light illumination, but occurs here when transmitted 850-nm light is used. The beam path, indicated by a red arrow, appears to go from the upper left corner to lower right, with a vignette-like effect in the other two corners. The two yellow arrows indicate an apparent narrowing of the beam width. The blue arrow in the center indicates the continuing beam direction. There is no ready explanation for those optical effects. The surface could not be properly resolved, as the bright flare would increase in size and brightness with decreased resolution. None of the available Zeiss cameras' or AxioVision adjustments proved effective.

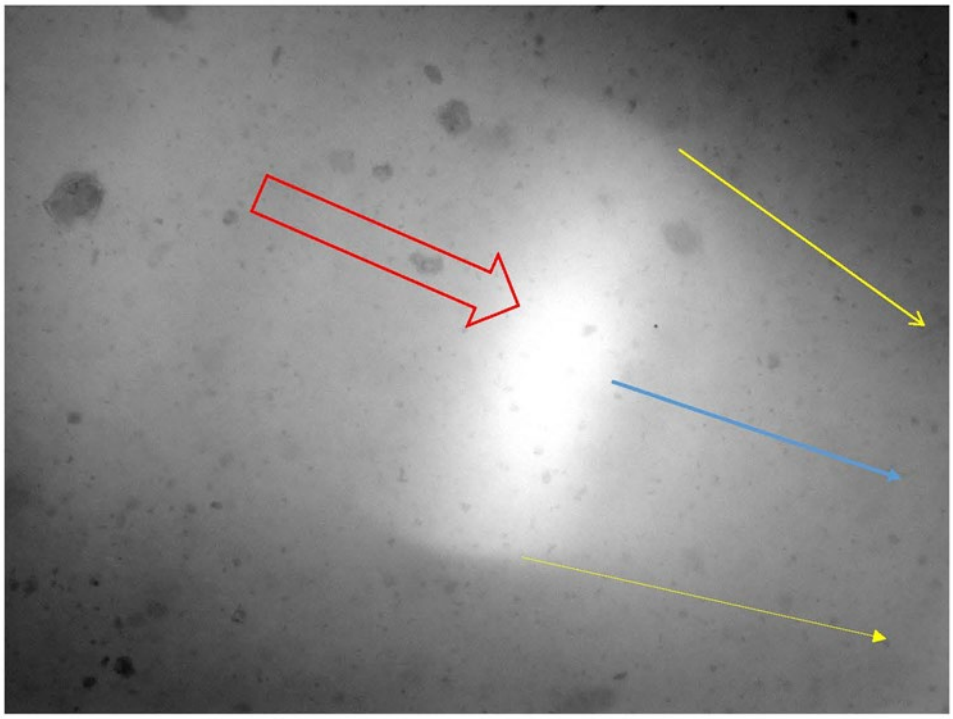

Fig. 30 Variation of the most frequent issue encountered using transmitted 850-nm illumination

Figure 31 is a variant of Fig. 30 with the specimen's surface distortions seen in the frame. These probably originated with light-beam distortions at the bottom aperture lens of a misadjusted condenser then interacting with the specimen internal microstructure. A variant not shown is a crescent-shaped hot spot, which is brighter than the surroundings, but not a white-out feature, similar to that in Fig. 30. That hot-spot shape, blue oval, only occurs in specimens that have the specimen edges accidentally illuminated. The two yellow arrows indicate a change in beam direction, accompanied by a flattening of the surface appearance. Anomalies such as these could be generated by internal reflections. A probable origin of the bumpy oblong shape is not clear, given the plane-like appearance moving to the lower right. For the Z2m to be the source of the optical anomalies shown, those same distortions also would have to occur when using white illumination, which they have not in 6 years of use.

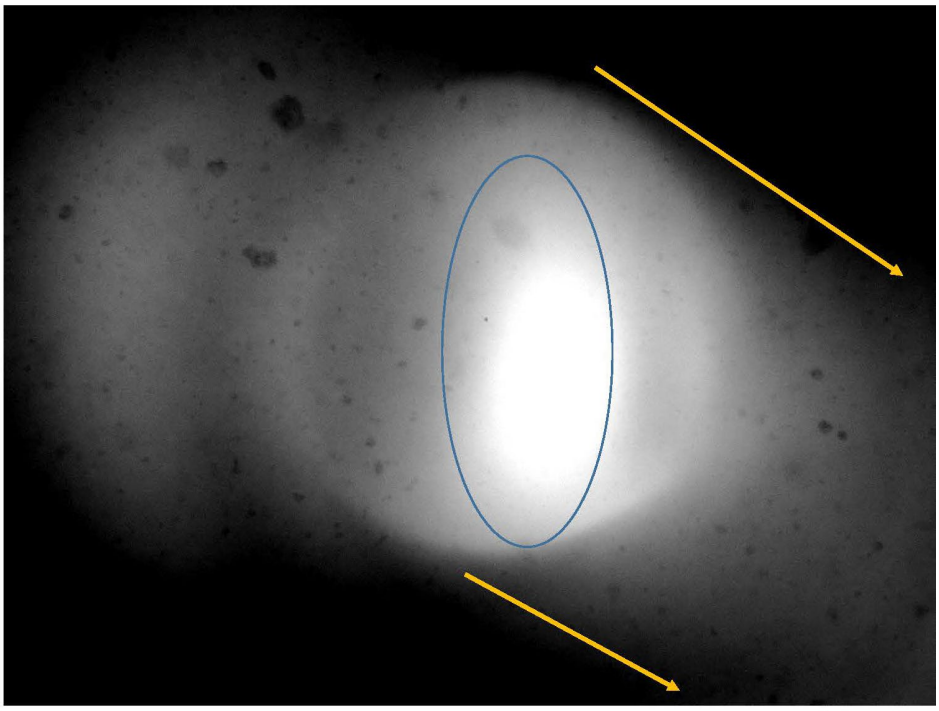

Fig. 31 Transmitted 850-nm variant of Fig. 24; note the nonconforming vignette-like appearance

A better understanding of these anomalies requires beam- and lens-modeling software, as well as the actual lens-design data for the Zeiss aperture lenses and possibly the objectives and camera projection lens. The lens data are Zeiss proprietary and would likely require the company's participation and possibly one of its research partners. Such an undertaking would require a priority to be established by ARL or another US Army Combat Capabilities Development Command element.

4. Comparison of 850- and 780-nm Illuminant Results

Four specimens, 4CC29-3, 1VB124-800, 2VB062, and 2VB063, were examined using both 850-nm and 780-nm illuminants. The initial 850-nm results for these specimens proved unusable as the result of the luminescent emission from the Er dopant (see Section 3.4). Specimens 4CC29-3 and 1VB124-800 received a limited comparison of results between the two wavelengths, and full re-analyses were not performed at 780 nm because they were no longer priority materials. These comparisons are presented in this section to highlight the improvements that were found by switching to the 780-nm source. The results of 2VB062 and 2VB063 are presented in Section 5, as no comparison between the sources was completed.

4.1 Specimen 4CC29-3

The available compositional data for 4CC29-3 list only Er and MgO (Table 1), which was the first MgO material tested using 850-nm illumination. Face 1 was polished and Face 2 was not polished; the latter is shown in the 50× reflected dark field micrograph (Fig. 32). Pull-outs appear to be present at random locations, but a definitive finding requires higher magnification that proved to be not possible. No transmitted light studies were performed on Face 2.

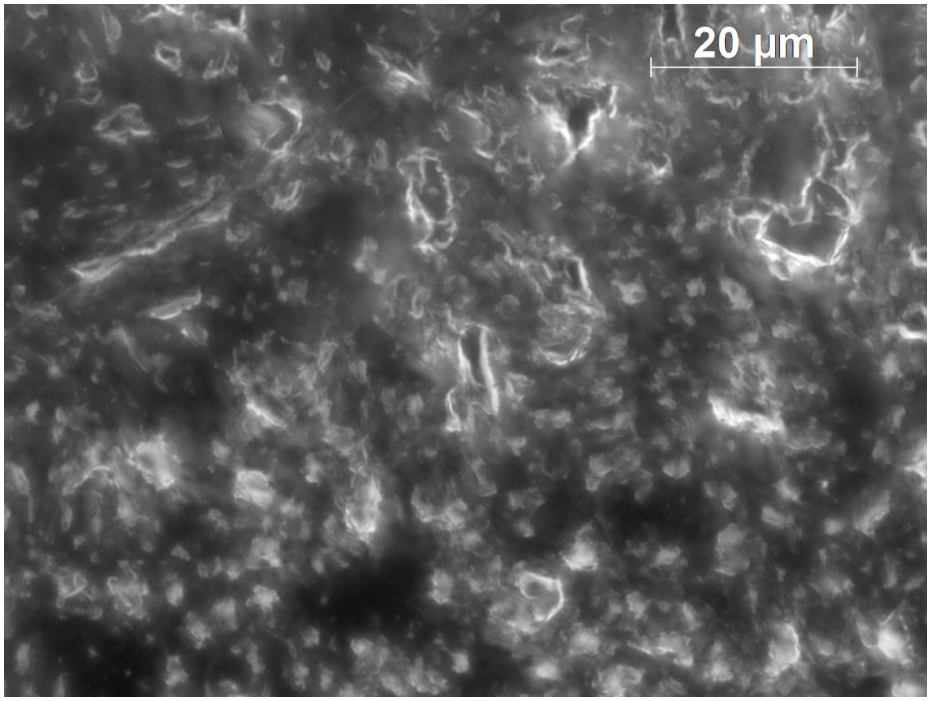

Fig. 32 Reflected dark field image of Face 2 for 4CC29-3 unpolished face

Figure 33 presents 4CC29-3, a series of polished Face 1 images employing a) 850-nm, b) 850-nm TBF using a color camera, and c) 780-nm illumination in that order for the 20× images. Figure 33a exhibits a higher contrast than Fig. 33b, giving the visual illusion of more detail. The use of a color camera in Fig. 33b demonstrates the Er fluorescence generated by the 850-nm LED's spectrum, as explained in Section 4.1. Figure 33c, using 780 nm, exhibits more surface details than in Fig. 33a, using 850 nm; the hot spot in Fig. 33a is greatly diminished in Fig. 33c, the result of no Er luminescence.

The monochrome camera's nominal spectral efficiencies (Fig. 3 in Section 2.2) shows about 22% efficiency at 850 nm and 43% at 780 nm. The nominal stated maximum beam powers are given as 400 mW at 850 nm and 180 mW at 780 nm (Table 4). The color camera's spectral range is 400–700 nm, with an IR cut-off filter.

The pink seen in Fig. 33b, using 850 nm, is not a spectral color as it does not possess a single wavelength band. Assuming red, 635–700 nm, is a major contributor to the observed color response in Fig. 33b, the relative chip response at 650 nm is above 0.8 (see Fig. 3 in Section 2.2), greater than two or three times the 850-nm relative response. Additionally, the recommended gamma setting for the color camera is 0.45 versus the monochrome unit's 1.00 gamma default setting. Those factors partially explain the observed different camera responses to the same specimen, as shown in Fig. 33.

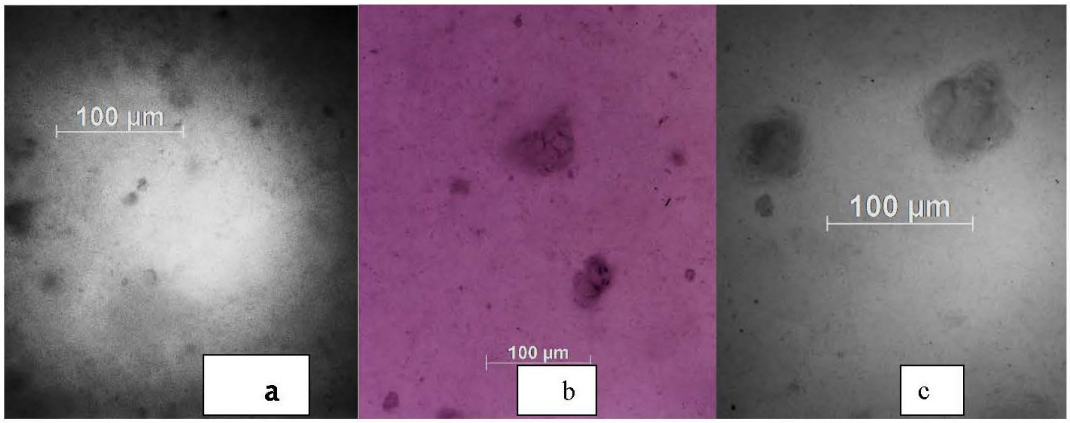

Fig. 33 Three 20× TBF images using a) 850 nm with the HRm camera, b) 850 nm with the color camera, and c) 780 nm with the HRm responses from the 4CC29-3 polished face; note difference between a) and c)

4.2 Specimen 1VB124-800-2

1VB124-800-2 is an air-fired Er:Y_2O_3 nanocomposite having both a polished Face 1 and an unpolished Face 2. The unpolished Face 2 was more readily imaged. There were attempts to fully examine both 1VB124 surfaces at 850 nm. 1VB124 is the first specimen recognized to be exhibiting Er fluorescence, but no response comparison was attempted such as that depicted in Fig. 33. Face 1 is covered in scratches, making the surface analysis tedious for specific areas. Figures 34 and 35 are both color images using RBF white light and TBF white light, respectively. RBF is good for surface morphology and to verify polishing as the reflected light is diffracted by the scratches and stands out against the undisrupted surface reflection, while the transmitted light, because it is not diffracted, will mask scratches on the exit faces. The entire study required TBF NIR for subsurface imaging. Here, the white-light TBF reveals possible transmission interferents. The white splotches seen in Fig. 34 do not correspond to any observable features in Fig. 35.

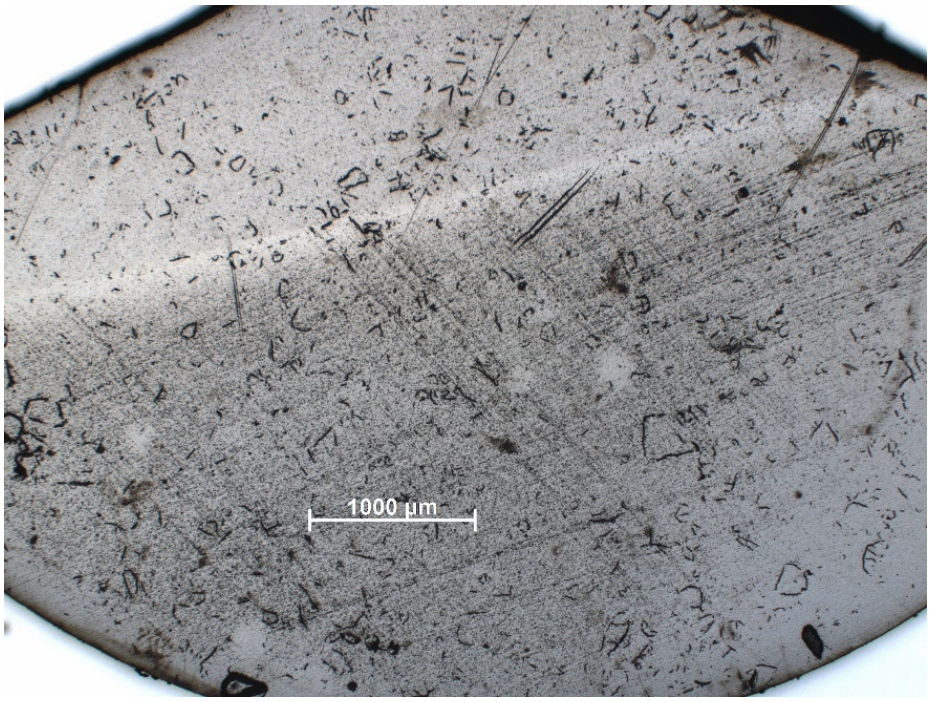

Fig. 34 RBF white-light color image at 2.5× of Face 1

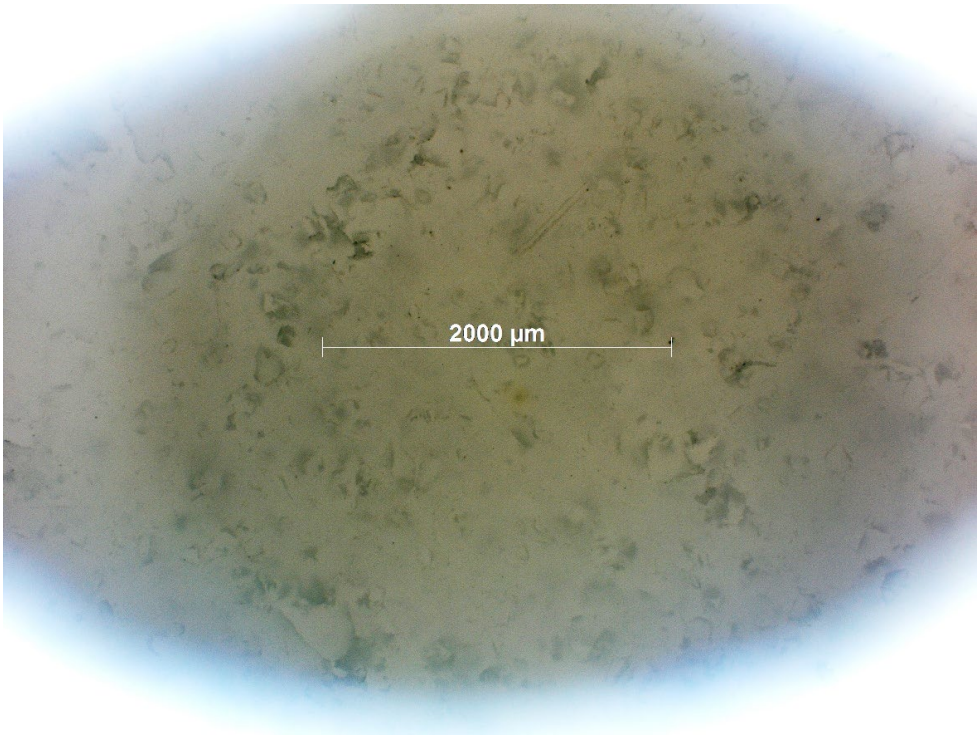

Fig. 35 Transmitted white-light 2.5× color image of Specimen 1VB124's Face 1 image

Figure 36 was made using RBF white light at 100×. It exhibits a degree of polishing that is void of visible grinding/scratching signs despite using RBF. At 100× the image can be taken between the scratches. Figure 36 shows the surface microstructure of the nanocomposite as well as the features and not the polishing processing. The area appears to lack any signs of debris. Note the white flecks/dots at the arrows are apparently embedded in the gray substrate, which was observed in other images.

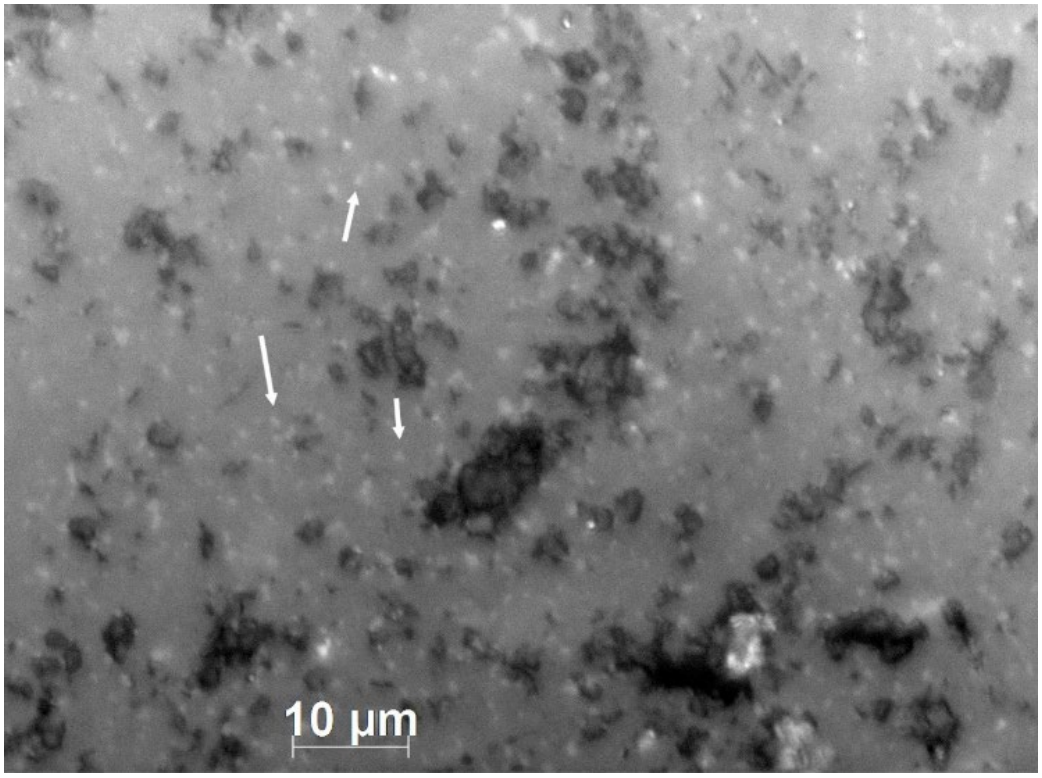

Fig. 36 1VB124's Face 1 surface at 100× RBF image, arrows noting more white spots in the gray matrix

The transmitted light imaging of the Face 1 surface proved extremely difficult, yielding only one poor-quality 20× image (Fig. 37). Despite the poor quality, the image shows the actual material surface structure and was synthesized from a 694-slice Z-stack for an indicated depth of 1019 µm. The rest of the specimens permitted Z-stack generations only between 2.76- and 79-µm calculated depths.

The bright area in the center of Fig. 37 is similar to the bright areas that randomly appeared in most specimens employing 850-nm TBF NIR illumination. These hot areas were seen at 10× to 100× magnifications, but mainly with the 50× and 100× objectives. Those distortions occurred mostly independent of the condenser and transmitted light-path settings.

The different density zones found in Fig. 37 evoke phase or species segregations similar to some images made using SEM backscatter. Their persistence in the center hot zone is more interesting, as they should be washed out by the brighter background. The effect may be the result of the grain orientations in this particular specimen volume.

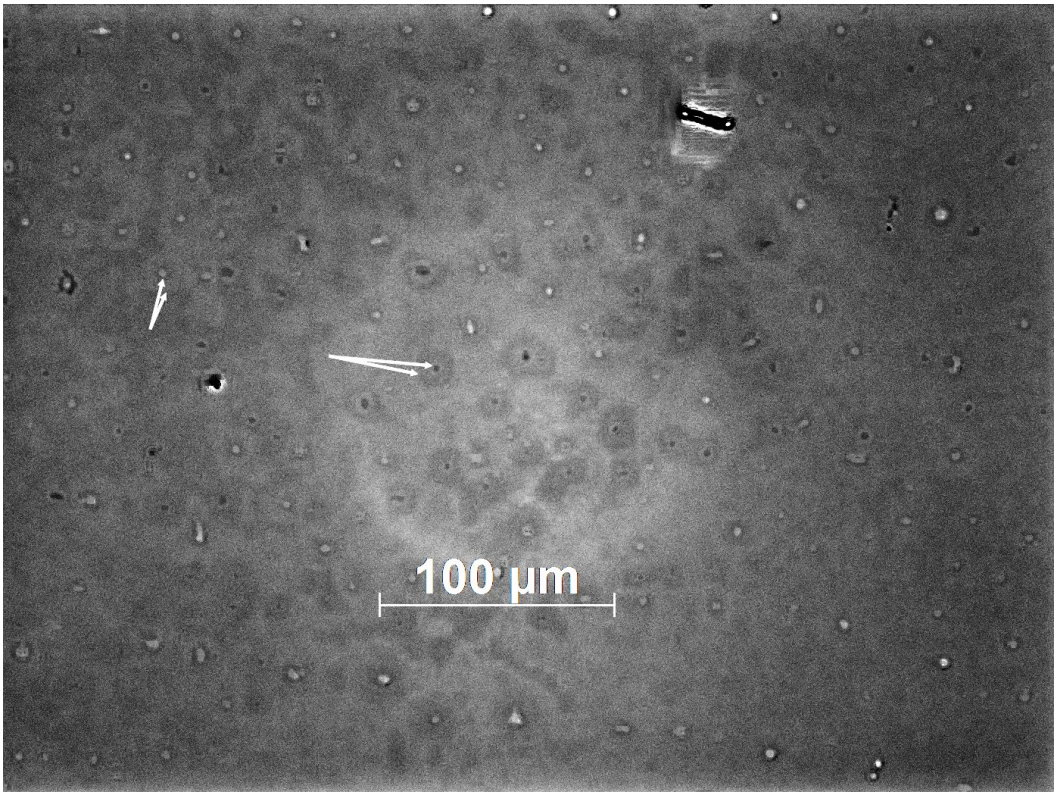

Fig. 37 20× TBF 850-nm NIR image for 1VB124 exhibiting a series of differing-density islands/zones, Face 1

The unpolished Face 2 in Fig. 38 demonstrates the Er fluorescence issue using the 850-nm LED (Fig. 38b) and the white light LED (Fig. 38a), both at 20× magnification. There is little difference between the two, which could only happen if the 850-nm response was over-augmented by the Er fluorescence response in the visible spectrum, 400–700 nm. Note the two surfaces exhibit a smooth film-like appearance, which can be caused by a fluorescent glow.

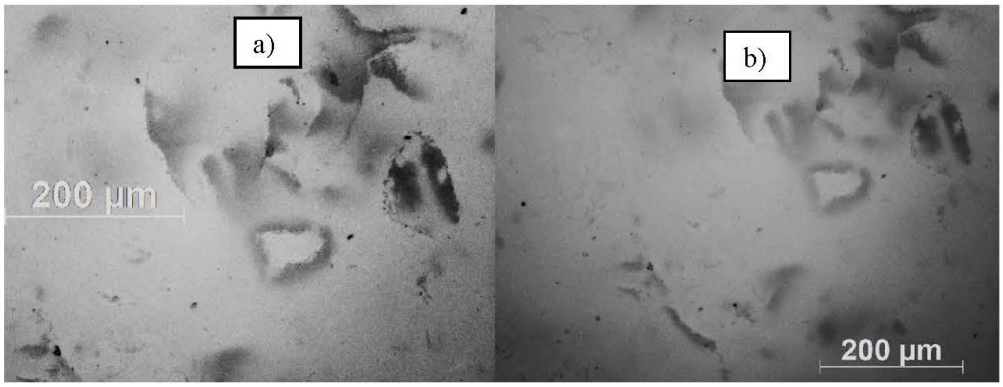

Fig. 38 Face 2 images of 1VB124 at 20× magnification using a) TBF white light and b) transmitted 850-nm light; note the film-like surface for both

Before switching to the 780-nm NIR source, a practicality test was performed using a medium-coarse sintered glass frit from ChemGlass and an Er:Y_2O–MgO composite specimen (Fig. 39). The first of the three-color images a) employed white light transmitted through the glass frit, b) used 780 nm for the frit image, and c) used 780 nm through a Er:Y_2O–MgO specimen. No fluorescence was evident from using a 780-nm LED at the nominal maximum beam power of 180 mW. The black object in Fig. 39c, above the scale bar, is an unknown surface defect blocking the through transmission of the 780-nm beam.

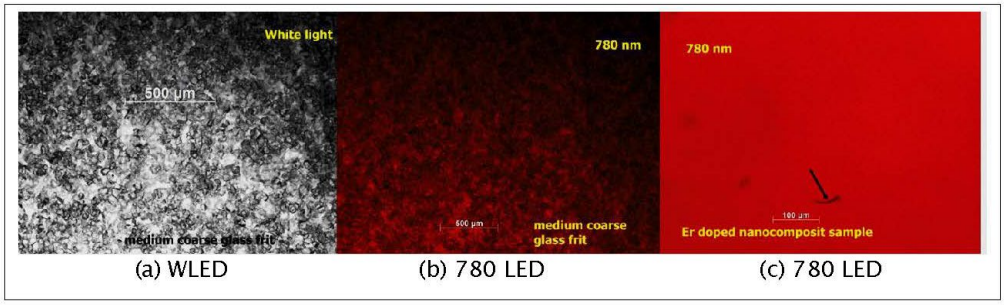

Fig. 39 Color images demonstrating the 780 nm does not generate a detectable fluorescent response from the Er: a) white light through a glass frit, b) 780 nm through a glass frit, and c) 780-nm LED through the Er-doped nanocomposite specimen

The unpolished surface of Specimen 1VB124, Face 2, imaged using the 780-nm source (Fig. 40) had fewer issues with transmitted illumination compared with transmitted white light or an 850-nm source. Polishing does not affect the fluorescence, making this comparison valid despite using the unpolished surface for the 780-nm source. Despite being air-fired, the unpolished Face 2 exhibits a film-like appearance with the transmitted light illumination. Retro-reflections from the objective may contribute to this result. No evidence of any NIR obscurant was

found. The feature indicated by the arrow maybe polishing debris from Face 1, while other similarly toned features could not be resolved.

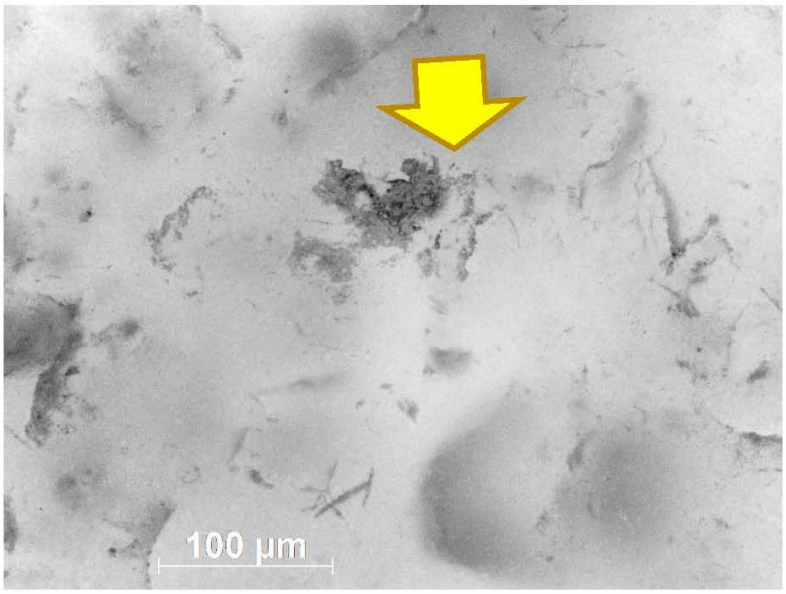

Fig. 40 TBF image of unpolished Face 2 of 1VB124 at 20× using 780 nm; no black flecks but other debris-appearing features (at arrow) are present

The 780-nm LED improved the HRm camera's capability to produce analyzable surface images, but not the capability to find any recognizable subsurface features for these two specimens.

5. 780-nm Results

The 780-nm source permitted NIR-based specimen exploration without the issue of optical interference from erbium-luminescence in the visible, 400–700 nm, using the HRm grayscale camera. The results described here are from specimens imaged using solely the 780-nm source and include 1VB113-400, 2VB059, 2VB062, and 2VB063. As mentioned previously, the latter two specimens (2VB062 and 2VB063) were also imaged using the 850-nm source, but the data were unusable. Again, both RBF and TBF illumination methods were utilized.

5.1 Specimen 1VB113-400

Unpolished and hot pressed, Specimen 1VB113-400, with a composition of 90-wt% MgO and 10-wt% Er:Y_2O_3, required two full optical examinations and an initial SEM study, proving to be the most difficult specimen to analyze owing to the inability to sufficiently illuminate the surface. There are two visually distinct zones on Face 1 as captured on the Phenom SEMs' internal cameras (Fig. 41),

which did not persist through to Face 2. Face 2 was the surface against the specimen holder and was not recorded in this fashion. Having been hot-pressed, the tone differences may be the result of graphite infiltration from the die into zone A. However, because both sides were in contact with the graphite punches, further explanation requires a disrupted BN film layer on one of the punches. Only cross-sectioning may provide the data needed for a clearer understanding of the cause.

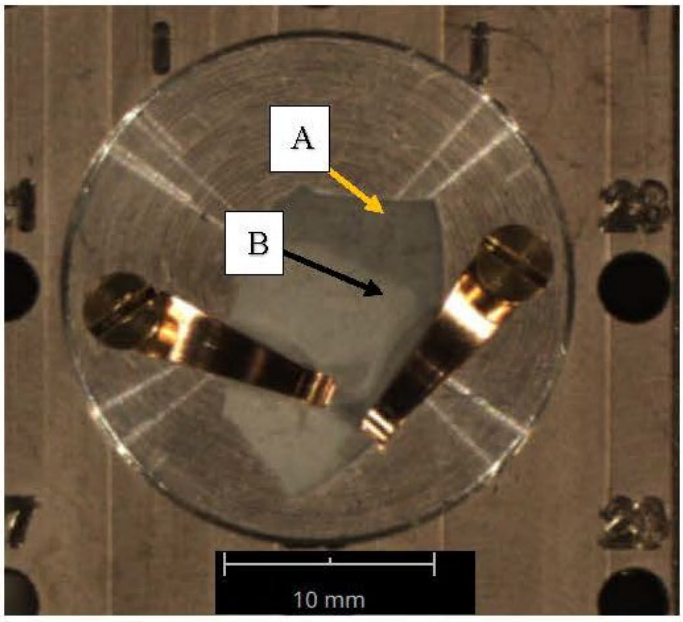

Fig. 41 Tabletop SEM camera image of 1VB113-400 on a 25-mm mount, Face 1, exhibiting two distinct areas, A and B

Use of reflected polarized light worked well for this specimen when employing RBF illumination. However, an unexpected reflected light-path malfunction precluded 5× and 10× imaging. The reflected polarized light produced clear images at 20× and 50×, Figs. 42 and 43 respectively. Figure 43 appears to be from different surfaces or areas, but is merely the crest of the large rounded feature on the left in Fig. 42 at the blue arrow. The yellow arrows in Fig. 42 indicate the rounded structures.

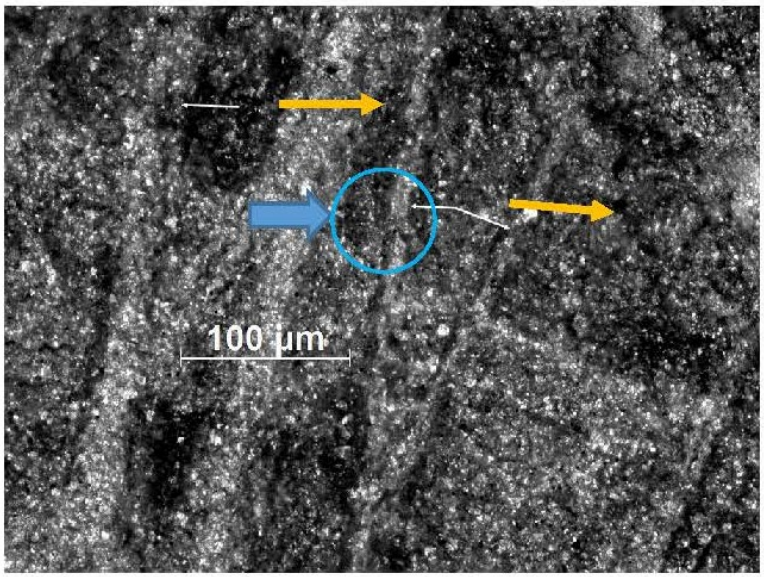

Fig. 42 20× reflected polarized light image of 1VB113 with several rounded structures at yellow arrows

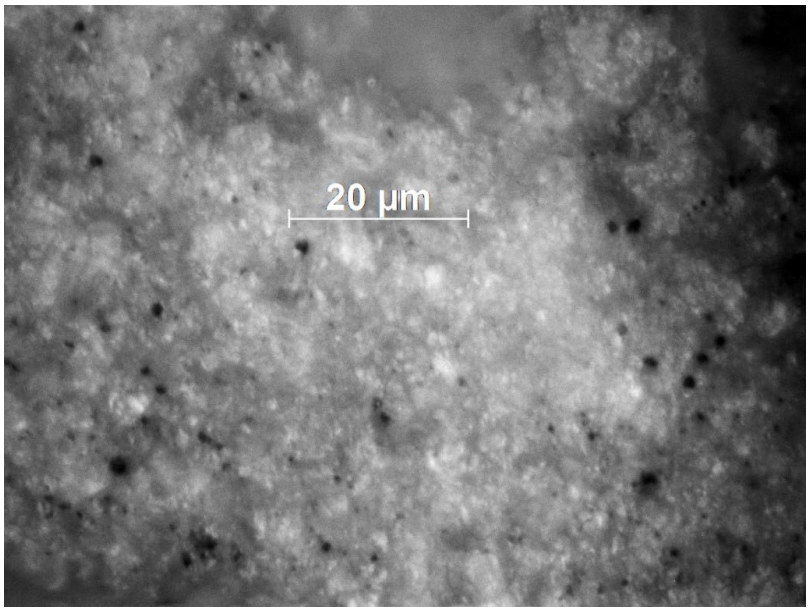

Fig. 43 Face 1 imaged at 50× using RBF polarized light; image region is located at the blue arrow in Fig. 42

The black flecks in Fig. 43 are consistent with the use of BN spray as a die-release agent during hot pressing. Figure 44 shows a 20× RBF image of a sprayed BN film surface on a glass slide. Three layers of the BN film were present on each side for a total of six layers, but not necessarily using the same brand of BN spray encountered during this study. Figure 44 shows a limited number of large agglomerates (i.e., black spots) similar to those seen in Fig. 43. The often-observed

black flecks appear to have been replaced by a series of very fine dots that are barely visible on the monitor but likely not that discernable in print.

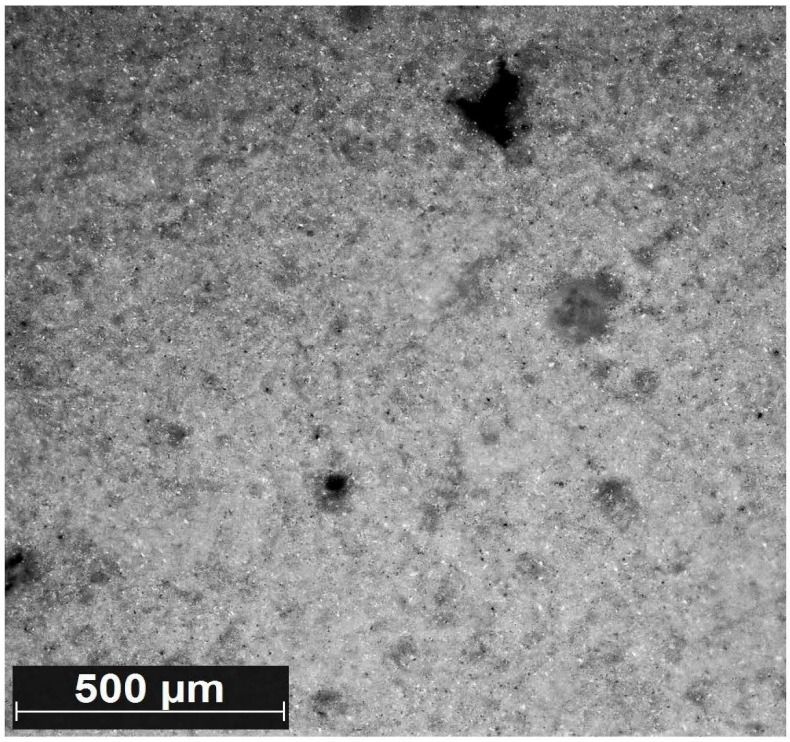

Fig. 44 20× RBF of a spray BN film on a glass slide

At 100×, reflected polarized illumination was used and the wavelet extended-focus algorithm unexpectedly produced improved sharpness (Fig. 45) compared with 50× (Fig. 43). Similar black flecks are present at both magnifications. However, at 100× individual white specks are seen (black arrows) as well as a node with several specks (white arrows). The large white arrow points out a small node populated by several white specks and the two yellow lines bracket the structure leading to the small node. The larger and smaller bright-white spots could be specular light reflections, which is likely given the short free-working distance for the 100× lens, 1 mm.

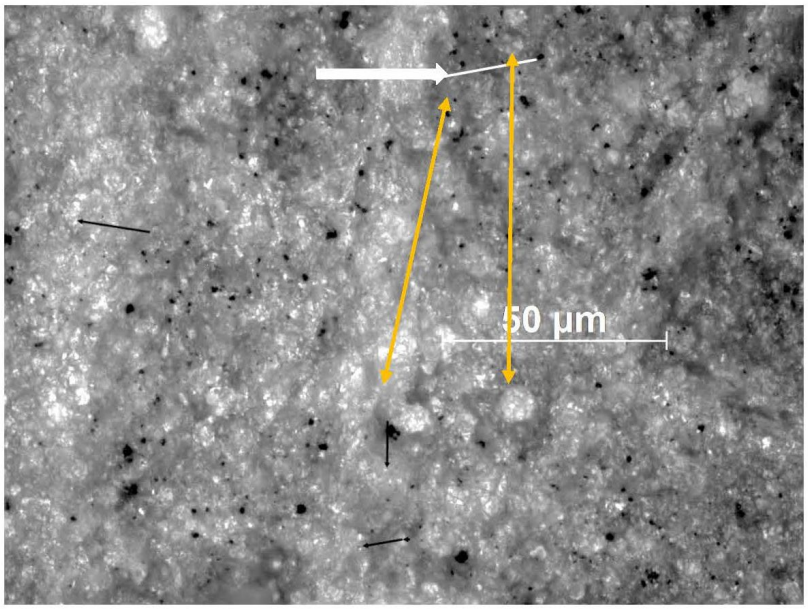

Fig. 45 RBF at 100× image of 1VB113

Nothing significant was revealed from the transmission of either visible or NIR light as is demonstrated by the 20×, 780-nm image shown in Fig. 46. Lower-magnification images were too dark for proper analysis, even with post-processing. The higher magnifications suffered similar issues. It is not known why the transmitted imaging was limited to only 20× magnification; the instrumentation is not available in-house to clarify the issue.

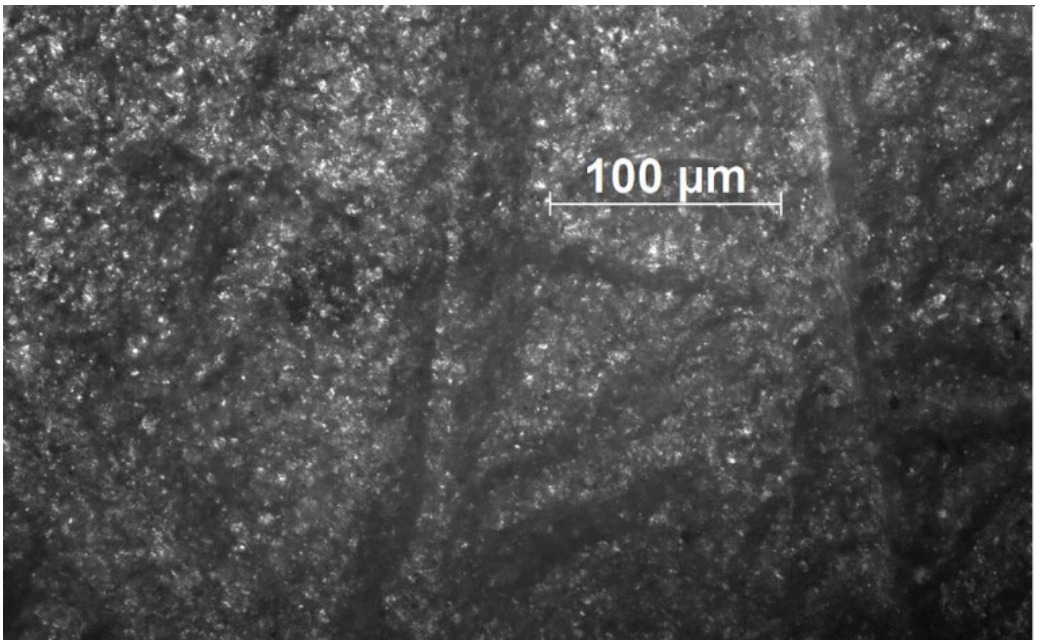

Fig. 46 20× postprocessed transmitted 780-nm light image of 1VB113-400

The SEM image in Fig. 47 displays a structural similarity to Figs. 42 and 43 with little additional detail, which demonstrates the validity of the optical images. The differences in frame appearances arise from comparing a RBF 50× frame (Fig. 43) with a SEM 3× frame (Fig. 47). The details within each frame are similar, just at a different magnification. The variation in surface morphology is in keeping with being a molded piece. The white arrows in Fig. 47 indicate the edges of three rounded structures. Remember, these rounded structures were also seen in the RBF images (Figs. 42, 43, and 45).

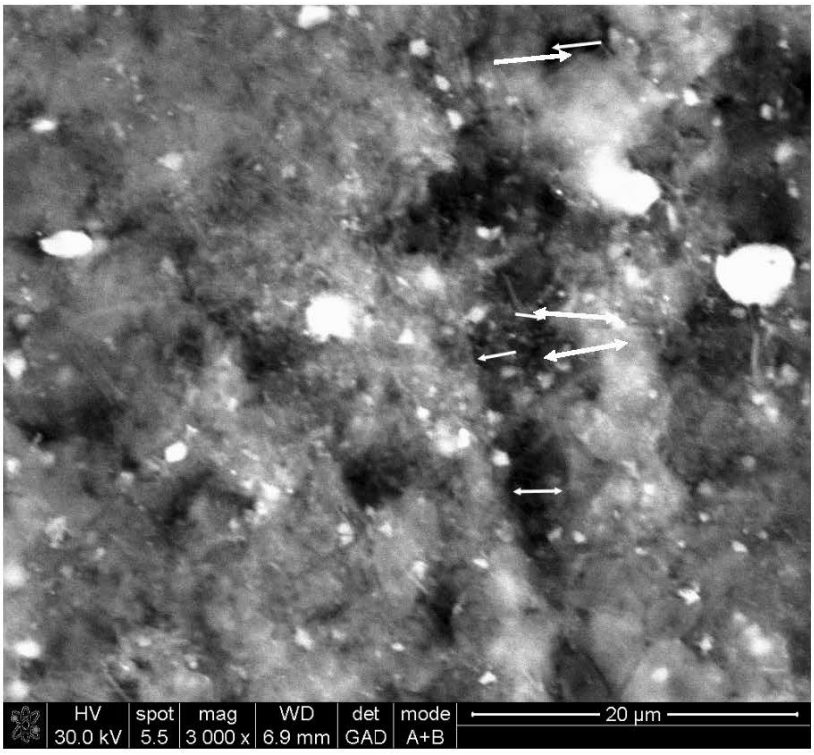

Fig. 47 SEM image of Specimen 1VB113 at 3000× exhibiting three rounded structures, with edges at the arrows

5.2 Fully Polished 2VB059

Specimen 2VB059 is a hot-pressed specimen with a composition of 96.5 wt% MgO and 3.0 wt% Er:Y_2O_3; processing details are listed in Table 1. On the highly polished Face 1, two zones are easily discernable, but not distinct, at 2.5× employing RBF white light with the HR monochrome camera (Fig. 48). The two zones are more distinct in the color image (Fig. 49).

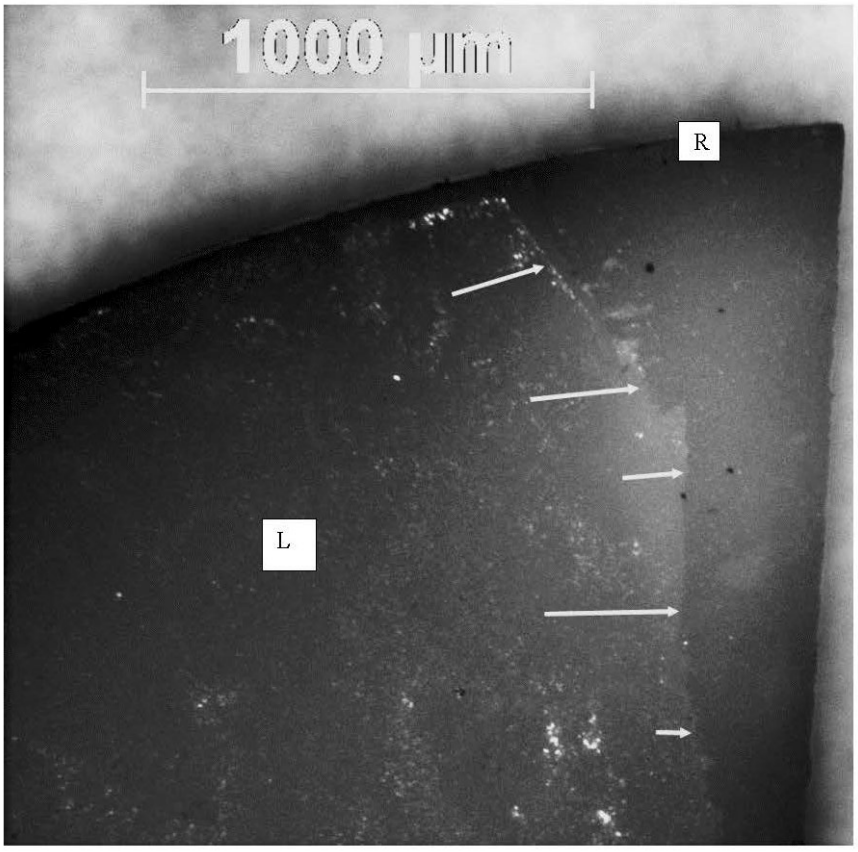

Fig. 48 2.5× RBF image from Face 1 of 2VB059 with two barely distinct areas indicated by the arrows at the common edge

The color camera outperformed its monochrome counterpart as indicated by the sharper delineation. A difference in microsurface roughness and subsequent light scatter is the most likely origin for the underlying color difference seen in Fig. 49. The purple hue is partially the result of 1) the camera's uncorrected white balance before the shot and 2) postprocessing contrast enhancement improving the image details.

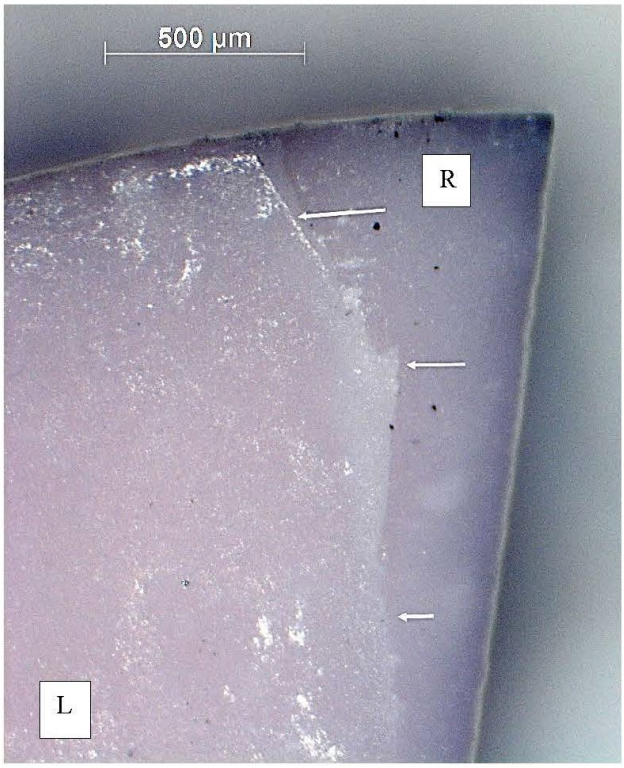

Fig. 49 Color version of Face 1, from Fig. 48 (2VB059 imaged using 2.5× RBF), provides an enhanced area differentiation

At magnifications greater than 2.5× the monochrome camera functioned well to bring out surface details for both Face 1 surface areas, left and right, using RBF. At 20× magnification (Fig. 50a), the area to the left now appears smooth, whereas Figs. 48 and 49 indicated it could be rough. The opposite is true for the area on the right side, which appeared smooth in Figs. 48 and 49 but appears to be rough in Fig. 50a. The 20× RBF image shown in Fig. 50b shows only the right-hand side of Fig. 50a, confirming the right-hand side is indeed rough. The physical structure of that roughness is likely reflecting the incident light, creating a smoothing light screen at 2.5× magnification that dissipates at higher magnifications (e.g., Fig. 50).

The yellow arrow in Fig. 50's Photo A marks a probable piece of yttria. In Photo B, the yellow arrow marks a large agglomerate. There are small white dots, indicated by the arrows in both Figs. 50 and 51, taken via 500× secondary electron micrograph. EDX mapping revealed these dots to be the yttria phases of the nanocomposite, similar to Specimen 2VB016 presented in Section 3.2. A separate report on the SEM–EDX studies performed will discuss the appearance and detectability of the yttria phase in more detail.

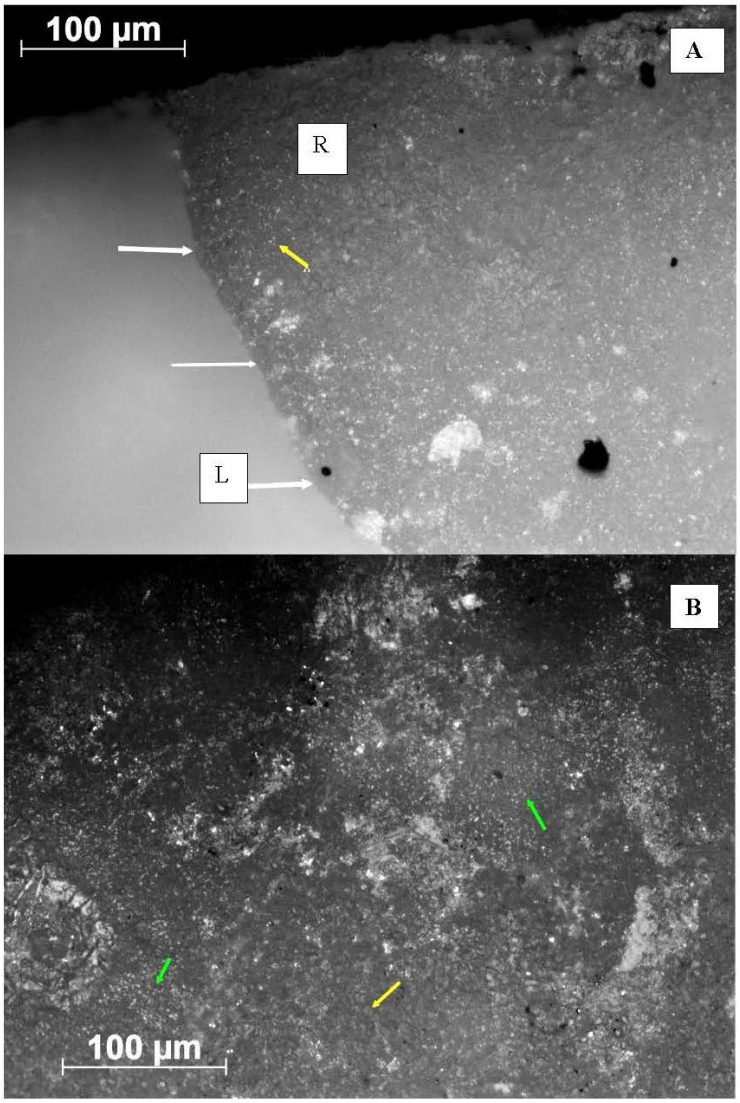

Fig. 50 (A) shows both Face 1 areas while (B) show only the right area, 2VB059; both A and B frames are RBF 20× reflected polarized light micrographs

The yellow arrows in the SEM micrograph of Fig. 51, 2VB059's Face 1, at 500× affirms Fig. 50's green arrows identify yttria pieces. The apparent surface tilt is not readily explained.

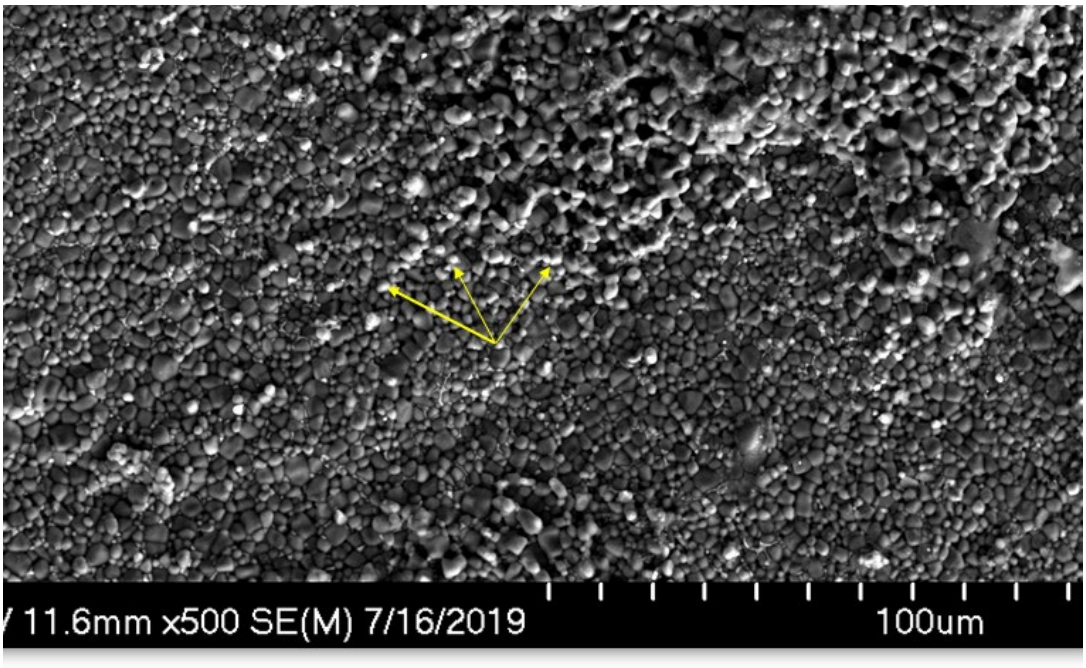

Fig. 51 Face 1 SEM micrograph at 500× of 2VB059 demonstrating the yttria phase appearing as white dots of varying diameters, indicated by yellow arrows

Figures 52–54 originated in the right-hand side of Fig. 52 and were derived using Z-stacks and the AxioVision extended-focus module's wavelet algorithm (both discussed earlier). The synthesized 3-D images mask the actual transparency of the whole area and, while very good, still did not allow for any real subsurface imaging, maximum focal depth being 74 µm. For the other specimens, the focal-depth range was 2.4 to 7.6 µm, largely the result of surface roughness or waviness, meaning surface to near-surface-only observations. The RBF micrograph at 50× of Face 1 (Fig. 52) exhibits contradictory features for such a small area, 180 × 135 µm. The large light-gray feature strongly resembles the surface of sticky rice topped with random pieces of foil-like material. The material appears similar to grinding debris—except it images too well for the most likely types of debris and the specimen was sonicated post-polishing.

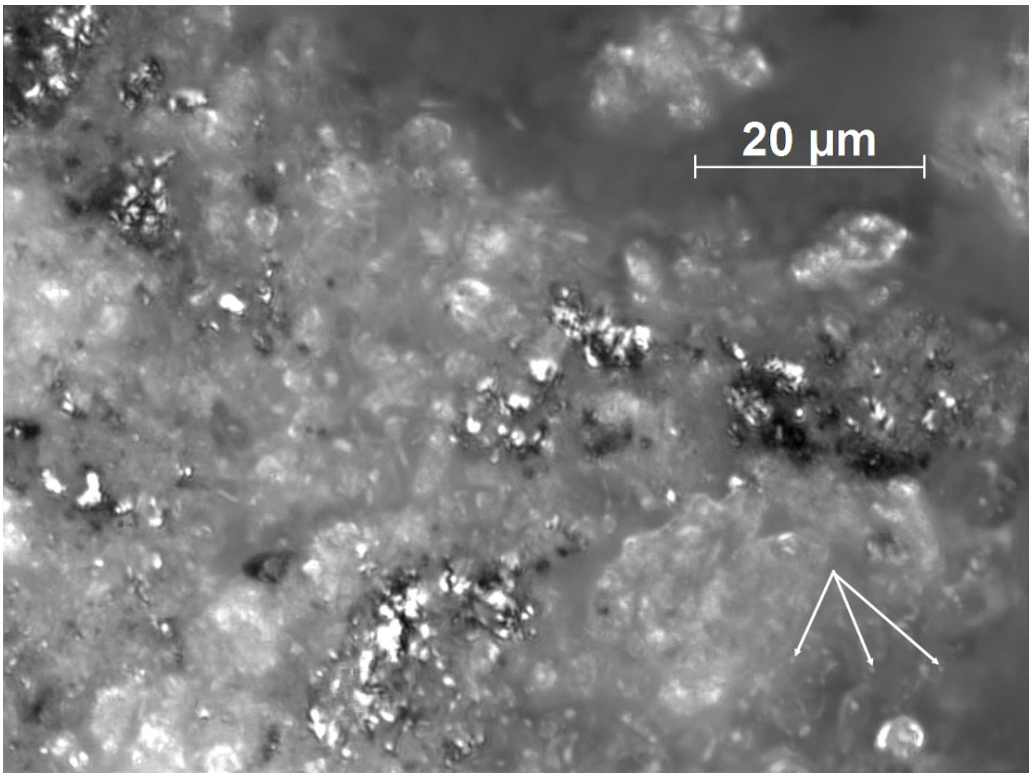

Fig. 52 50× RBF 2VB059, Face 1, image showing metallic-like clusters, nodular light-gray structures, and white spots at the arrows

Figure 53 is an RBF image of 2VB059, Face 2, at 50× magnification. This image also exhibits contradictory features for such a small area, 180 × 135 µm, but they are not the same as for Face 1. The large medium- to light-gray feature strongly resembles dry mop lint with entrained black debris or agglomerates and slightly darker-gray small, round pebbles, the latter extend on to and across the white surface. Face 2 became buried when the specimen was mounted on a SEM mount; hence, no SEM images or energy dispersive spectroscopy elemental maps could be obtained.

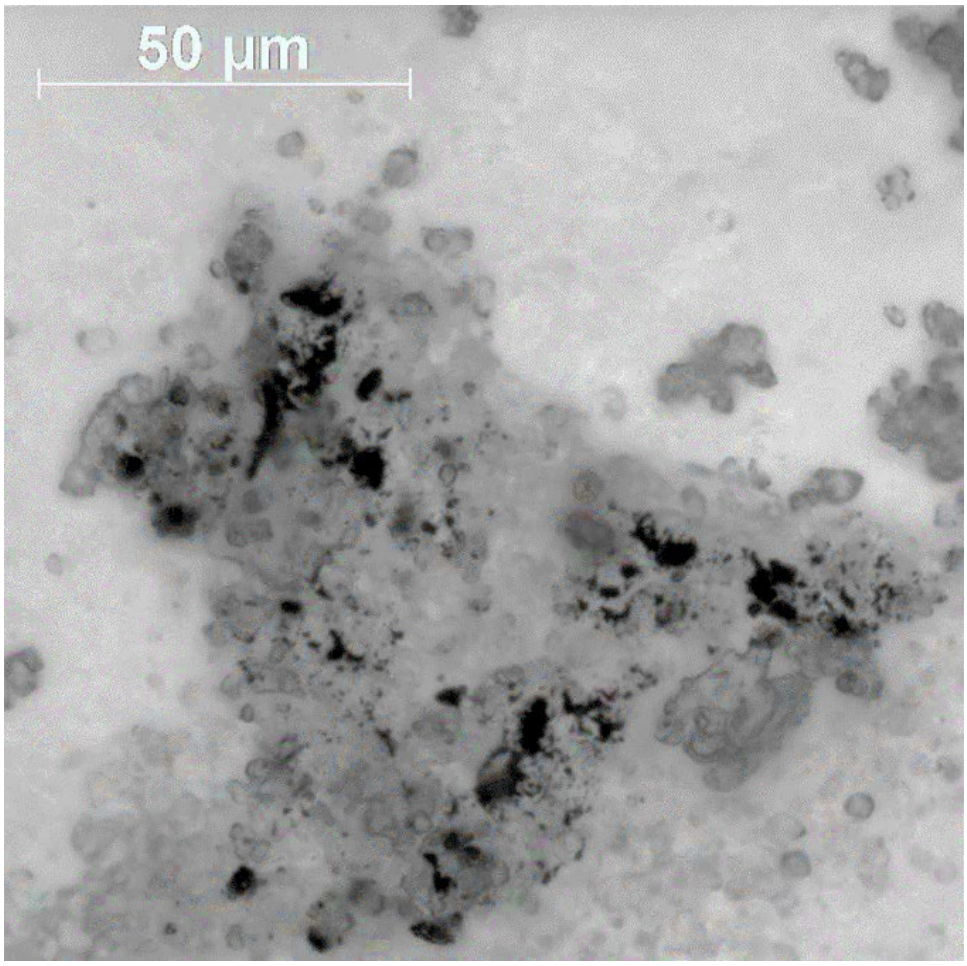

Fig. 53 RBF optical image at 50× magnification of 2VB059's Face 2; unknown material is shown on the surface, possibly grinding debris

The photo in Fig. 54 was taken in an area adjacent to the area shown in Fig. 53. The large dark clumps seen in Fig. 54 and indicated by the black arrows, Face 2 using TBF 780-nm light, are similar in appearance to agglomerated debris. The abundance of black spots/flecks on the Face 2 of 2VB059 was surprising, but their presence is not. At the time, one of the BN sprays readily deposited black flecks but not in the density seen in Fig. 43 nor in the clusters observed on Face 1 (Fig. 52), which opens the possibility of processing debris, which can easily reattach to the surface due to van de Waal's forces during sonication. The blemishes at Fig. 54's yellow arrows indicate a possible near-surface feature from an agglomerate or a change in local density, grain size, or orientation. Not all blemishes are marked in the figure. Cross sections through the specimen at those locales with the use of EDX mapping are required to resolve the exact nature of both the black agglomerates and the medium-gray features seen in Fig. 54 at the black and yellow arrows.

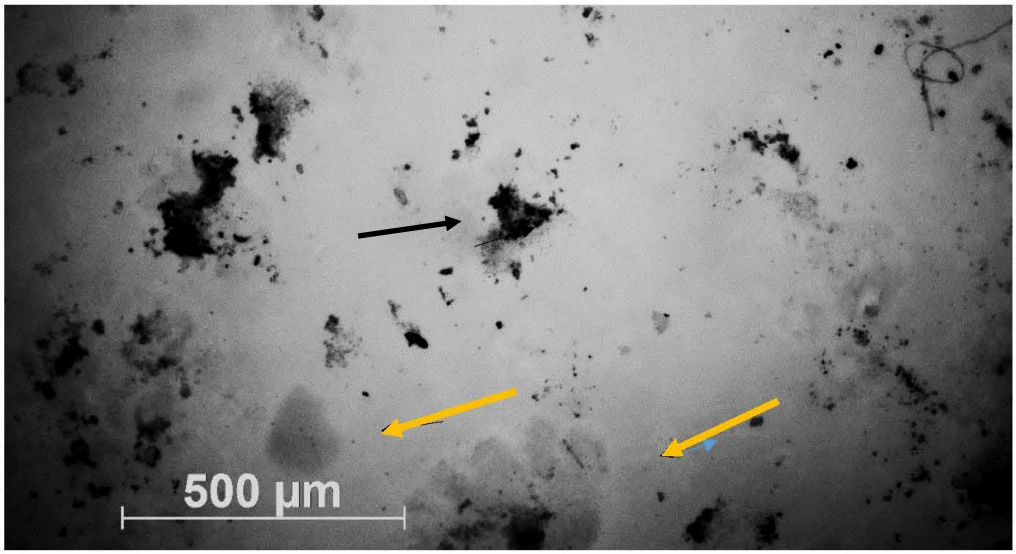

Fig. 54 780-nm 20× TBF Face 2 image of 2VB059 showing large debris field of agglomerated black articulates indicated by black arrow (center of photo) and apparent near-surface agglomerates at the yellow arrows

A TBF image of a sprayed BN film surface on a glass slide was not possible due to pinhole flaring with transmitted NIR, which limits available light adjustments. Thus, a comparison of those agglomerates with the current micrograph could not be made.

The TBF of Face 2 of the 2VB059 specimen at 20× magnification, shown in Fig. 55, contains several lines of fleck-like features from lower left to center and then branching upward. Both the act of spraying and act of polishing can create such patterns as well as the agglomerates seen at high magnification. For unpolished surfaces, those contaminants serve as a focusing aid for microscopy, but the extent of possible interference with a transmitted coherent beam is problematic. On polished surfaces, they have the potential to diffract a coherent beam and/or induce localized heating. The white arrows indicate potential polishing direction.

The black flecks are reoccurring artifacts on a number of specimens, but the agglomerates in Fig. 55 were a specific area occurrence rather than a recurring issue. Also present in Fig. 55 is the vignette effect, which is unusual with the 20× objective. For polished faces (i.e., Face 1), black flecks could be grain pull-outs, but Fig. 55 is an unpolished Face 2.

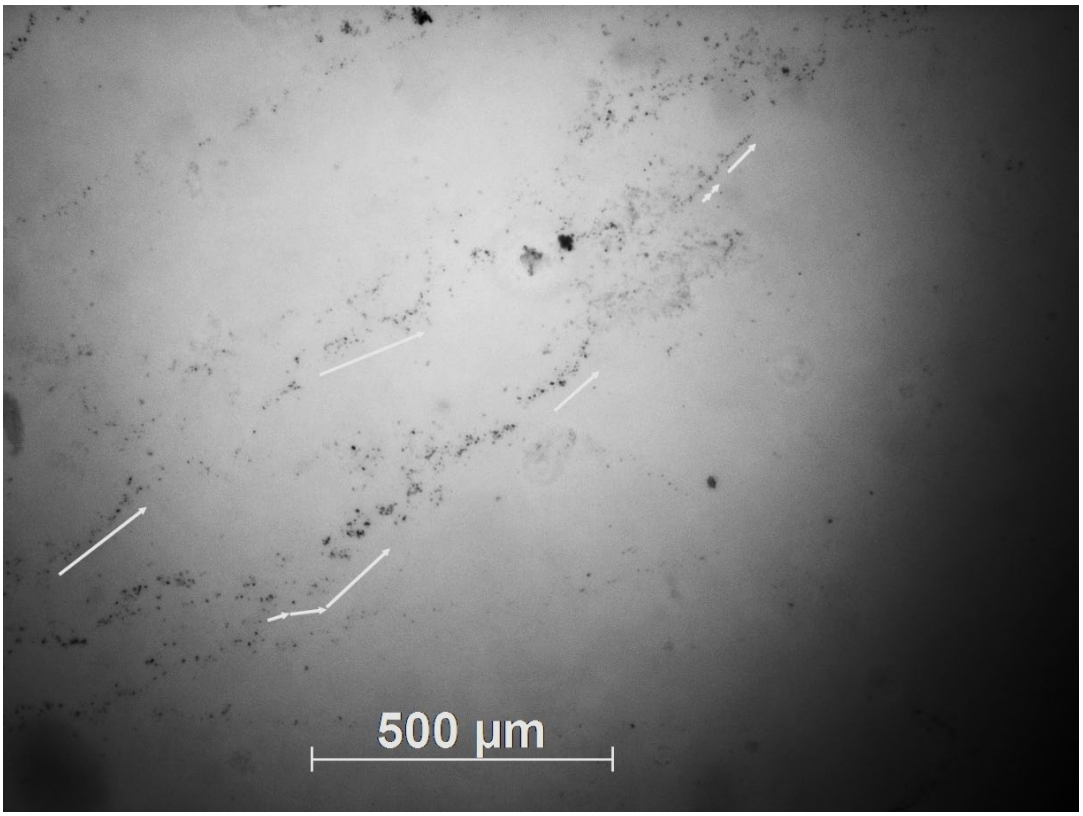

Fig. 55 2VB059's Face 2 at 20× using TBF monochromatic 780-nm NIR

The optical surveys of 2VB059 revealed a series of interesting features not readily explainable by optical methods that may not be relevant to the desired end function of the nanocomposite. Some of those features do indicate a need for better specimen handling rather than relying on polyethylene plastic bags.

5.3 2VB062 Results

Specimen 2VB062 is a hot-pressed nanocomposite composed of 96.5 wt% MgO and 3 wt% Er:Y_2O_3. Reflected white light was employed to document the topographical differences between the polished Face 1 in Fig. 56A and the unpolished Face 2 in Fig. 56B. At 10× magnification, Fig. 56A shows some polishing scratches, what appears to be a fracture line from sectioning the original whole disk, and a white-appearing splotch. Face 2 in Fig. 56B at 50× was imaged using the color for clarity. The high-resolution monochrome camera could not resolve the 50× scene. Figure 56B appears to have a large white phase, possibly residual BN film.

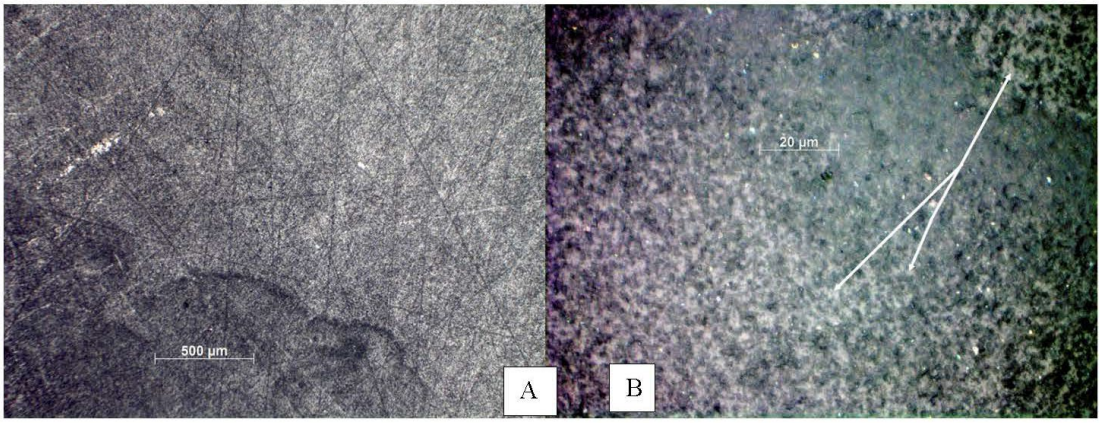

Fig. 56 RBF images (left) Face 1, fully polished with polishing lines at 10×; (right) Face 2, unpolished/no-polishing lines present at 50×

Transmitted 780-nm bright-field illumination readily captured surface contaminates or pullouts on Face 1 (Fig. 57A). Figure 57B, an SEM micrograph, reveals no apparent surface contaminants. The two photos are not from the same fragment. At magnifications less than 3000×, most porosity would not normally be seen.

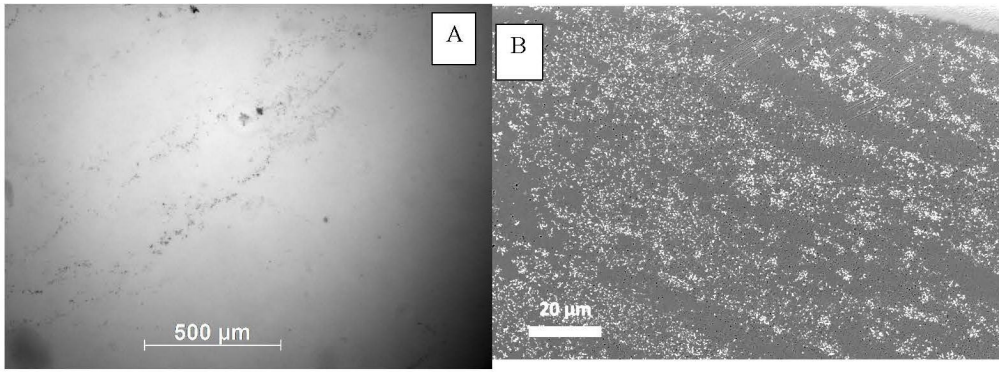

Fig. 57 (left) 10× optical image of 2VB062's Face 1 using 780-nm TBF and (right) backscatter electron microscope's image of 2VB062, in which the lighter phase is Er:Y_2O_3 and the darker phase is MgO

For 2VB062, black flecks and not pull-outs are evident on the polished Face 1 (Fig. 58a), while the unpolished Face 2 (Fig. 58b) reveals the BN–substrate interface. The unpolished Face 2 is imaged looking through the nanocomposite from Face 1 to composite–BN film interface on Face 2. The orientations of the nanograined MgO–Er:Y_2O_3 composite volume and the 780-nm wavelength cause the fuzzy appearance. The variations in tones, dark to light, arise from thickness differences in any BN film that are amplified by the quantum spectral efficiency of the camera chip at 780 nm.

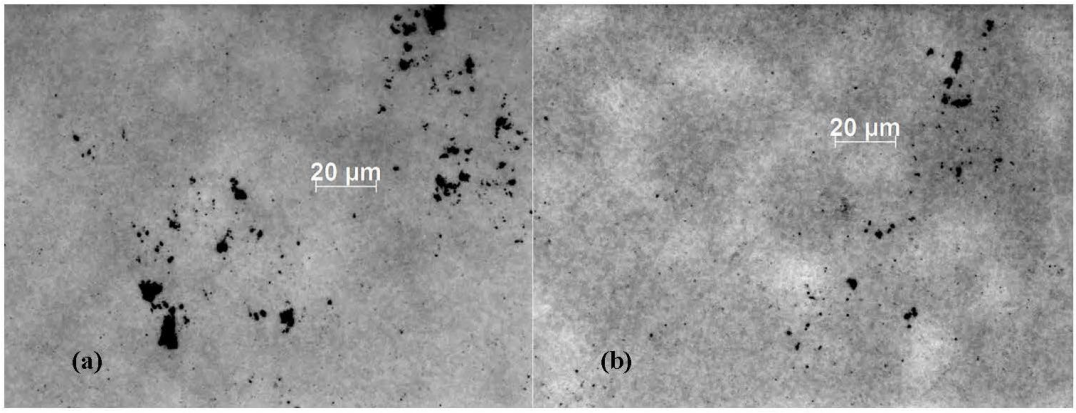

Fig. 58 Transmitted 780-nm images of the a) polished Face 1 of 2VB062 looking through the specimen thickness to b) Face 2

Again, in Fig. 59, the transmitted light is incident on Face 2 with the black specks residing of the surface of Face 1. The BN–nanocomposite interface is more clearly defined, demonstating the transparency of the specimen bulk volume. Figure 59 was cropped to improve the resolution of the interface on Face 2.

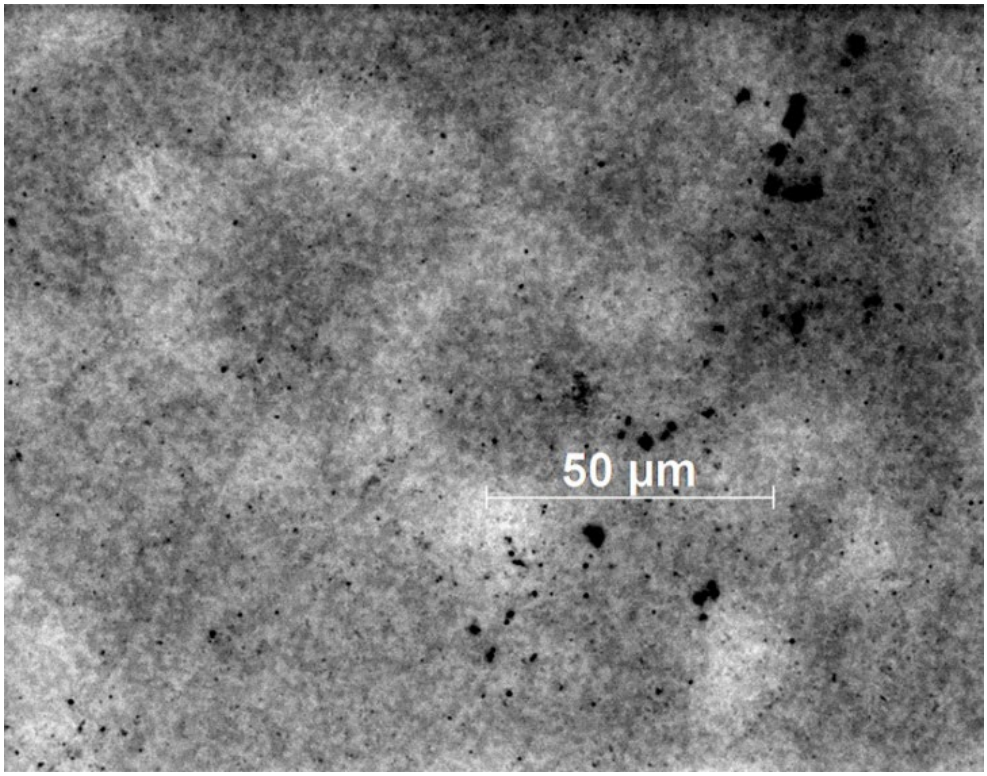

Fig. 59 2VB062's polished surface with foreground debris sharp and the far Face 2 BN–ceramic interface again appearing fuzzy

Figures 58 and 59 are direct proof of the clarity of the nanocomposite but not the degree of clarity. The finer dimpling reflect the surface structures of the Face 2 substrate proper and are similar to the Face 1 morphology when using reflected light.

5.4 2VB063 Results

Specimen 2VB063 is a hot-pressed 96.5 wt% MgO with 3 wt% Er:Y_2O_3 specimen. (See Table 1 for more details.) 2VB063 was examined twice using both 780-nm NIR and white light, first as a partially polished full disk producing no usable images. One face of a fully polished fracture segment was coupled with a second face compromised by the use of a black marker. The viewing Face 1 area above the location of that mark was readily avoided. Working with the fractured 2VB063 specimen required reflected white light at 20× and 50× to distinguish between the two faces of the specimen to reaffirm there was polished face able to be analyzed.

The RBF 10× micrograph in Fig. 60 appears to include both bare substrate and areas of residual BN film. Moving lower along the specimen disk's perimeter, in Fig. 61, the surface appears cleaner at 10× magnification, possessing a finely pocked surface in contrast to the roughness observed in Fig. 60. The average roughness variant, lying somewhere between those two images, is readily observable but unquantifiable using this scope.

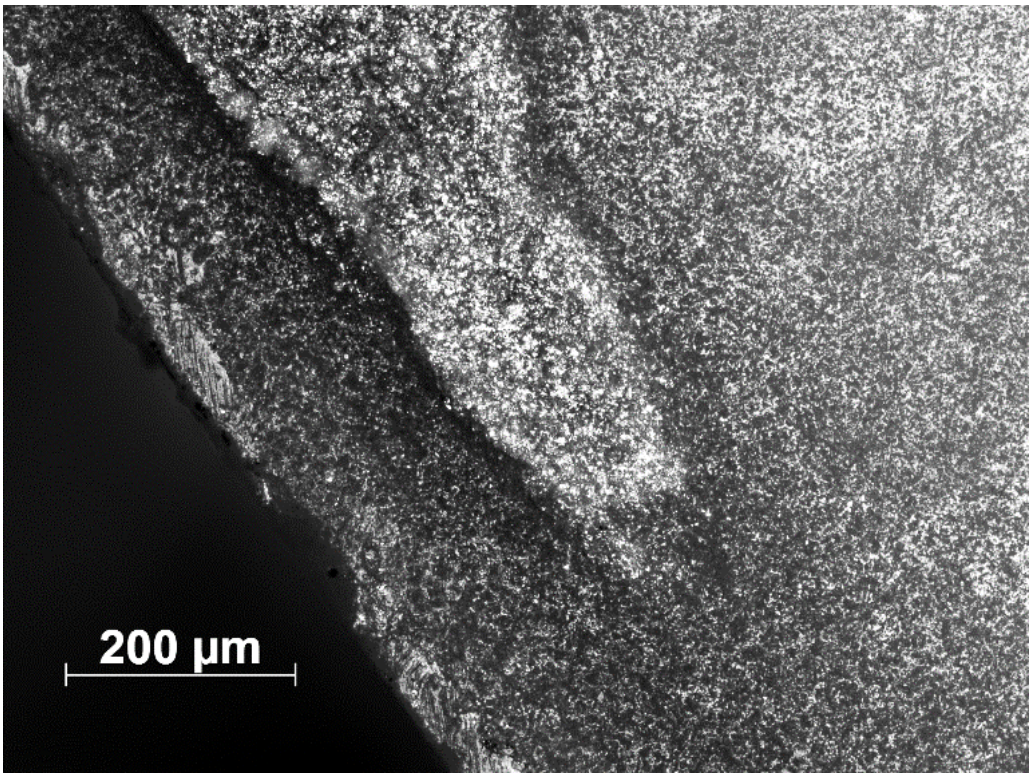

Fig. 60 10× RBF, Specimen 2VB063

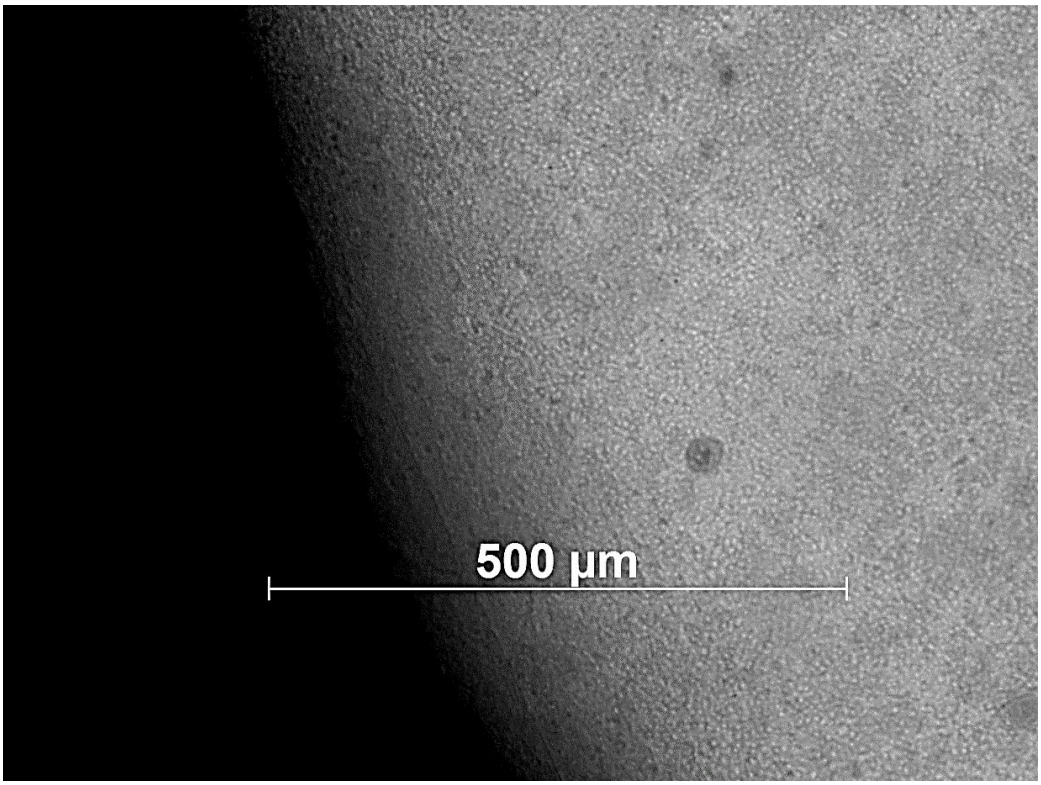

Fig. 61 10× image lower down the specimen perimeter from the first analysis (Fig. 60)

The next three micrographs, two at 100× and one at 50×, provided a quick overview of the variability of the Face 1 surface. Figure 62 depicts one 100× RBF image with a mostly cleaned surface with some apparent residual BN. The white dots (some noted by the white arrows) were later identified as yttria pieces. The chunky material upper right may be uncleared polishing debris that was pushed along the surface rather than being lifted completely off the substrate.

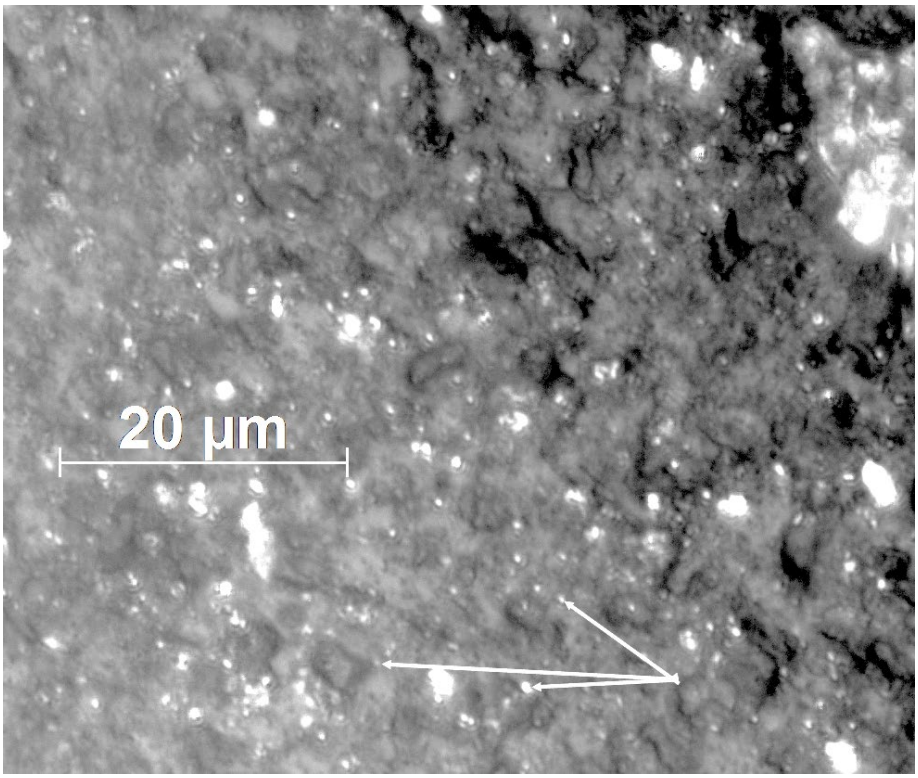

Fig. 62 100× RBF looking at a different area on Face 1; yttria dots of varying diameters noted

An example of what was the unpolished specimen face is imaged at 100× in Fig. 63. A possible residual film appears to dominate the image. Reducing the magnification to 50×, in Fig. 64, reveals a more mixed topography that is not readily explained by optical methods. The darker MgO phase appears to occupy the major portion of the image, which was later confirmed by EDX spot analysis.

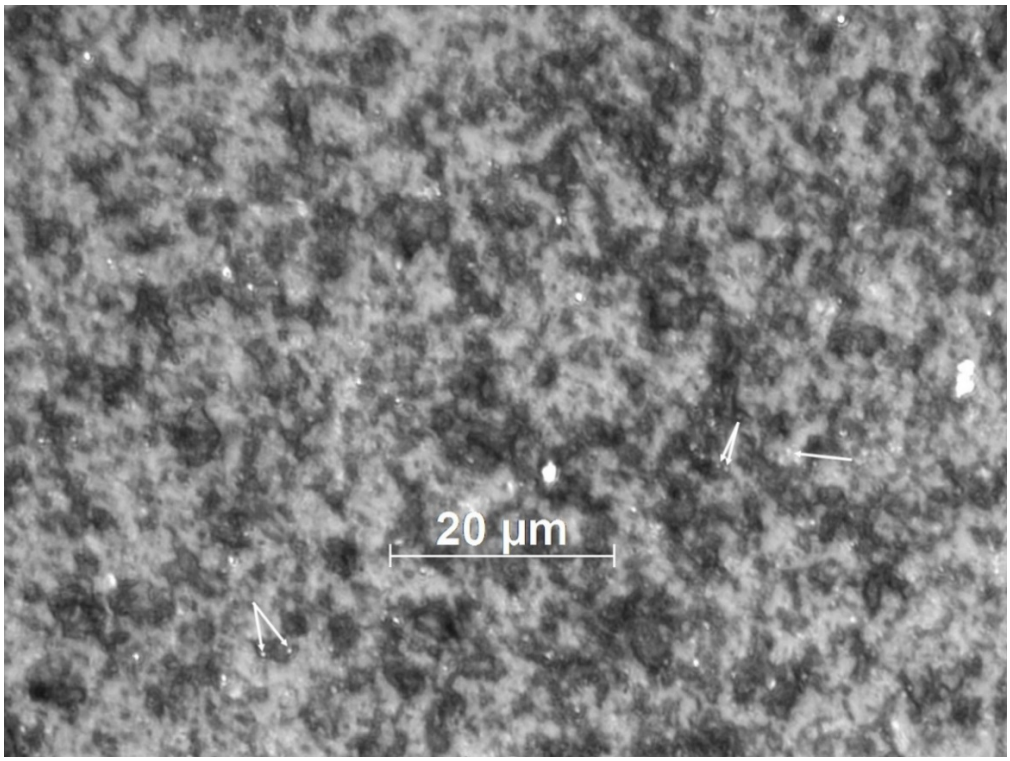

Fig. 63 100× view of what appears to be light-colored material in different area of the then-unpolished Face 2, RBF; note white spots, indicated by white arrows

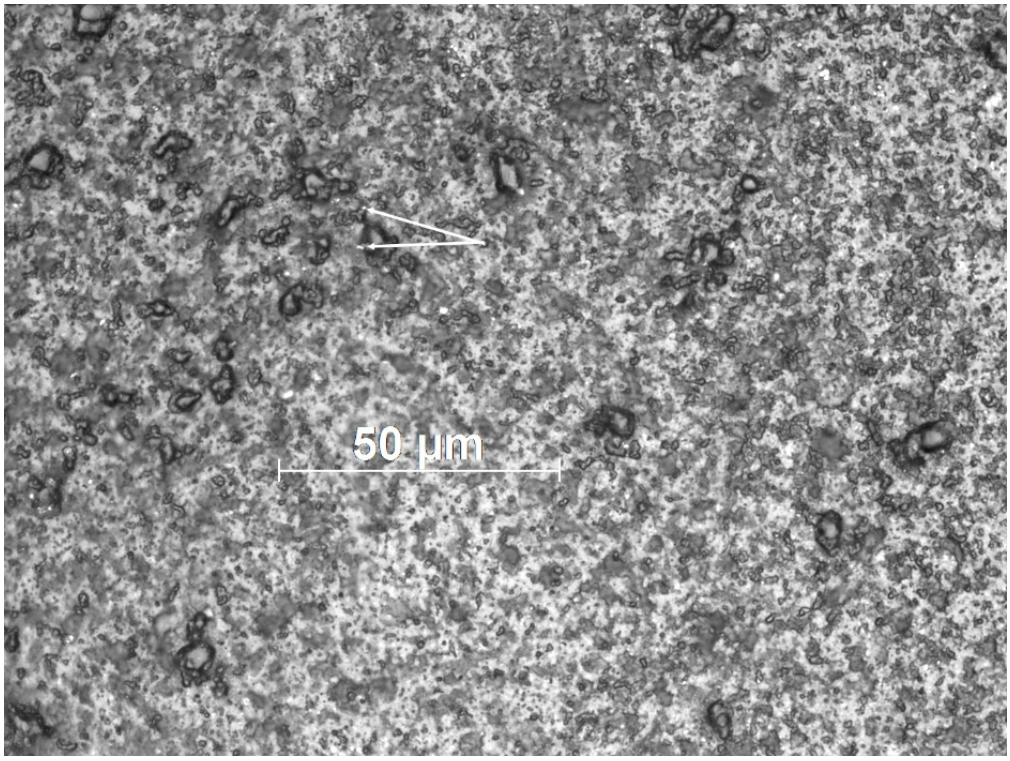

Fig. 64 50× RBF image of Fig. 63, polished Face 2 area where extent of the white material is better defined

The 10× TBF image in Fig. 65 captured a number of black flecks residing on what appears to be a film surface. This surface does not possess the fuzzy characteristics of the “far” face film in Figs. 58 and 59, but is not well defined. Note that those flecks appear to lie on a plane and do not conform to the underlying morphology of the unpolished surface. Here the low-magnification image can readily deceive the eye. The hot spot in Fig. 65 inhibited refining the micrograph further.

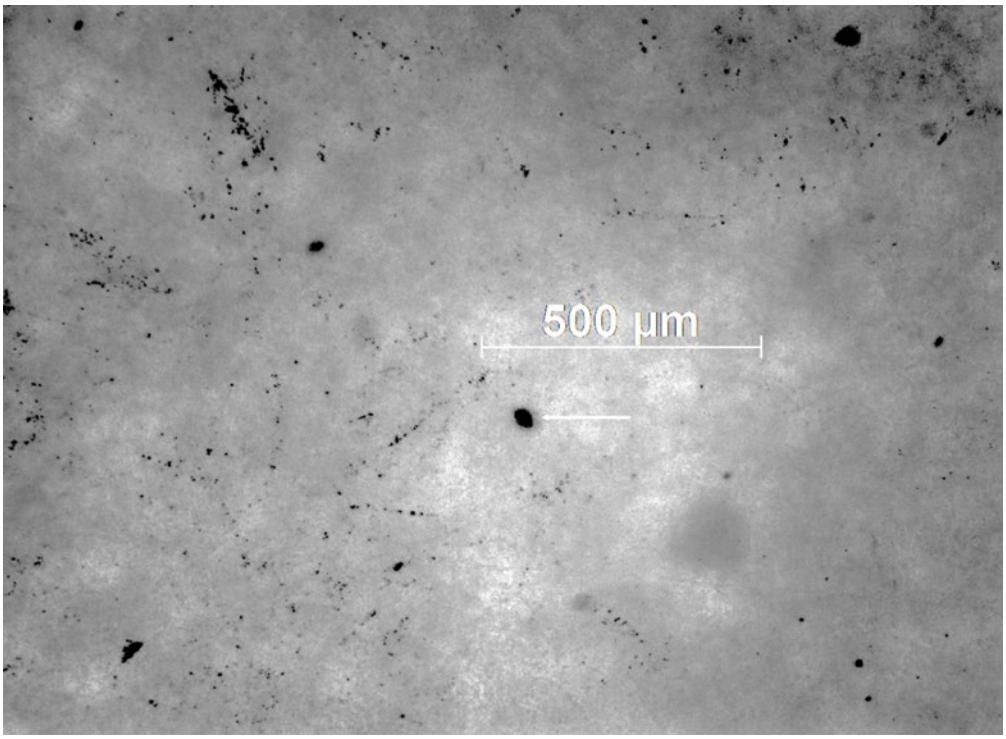

Fig. 65 10× image taken using 780-nm TBF of BN film on the Face 2 of 2VB063; black specks lie on mottled unpolished-specimen surface

Figure 66, Face 2, illustrates the optical deconstruct of a large black dot first observed at 10×, as seen at 20× and 50× using transmitted light. This is the only instance of a Z-axis clustering-coalescence result that could be a through-transmittance interferent for coherent beams if found in the nanoceramic matrix. There is an optical coalescence of smaller individual spots to form an optically larger light-blocking area. Identification of this type of feature subsurface was the basis of this study.

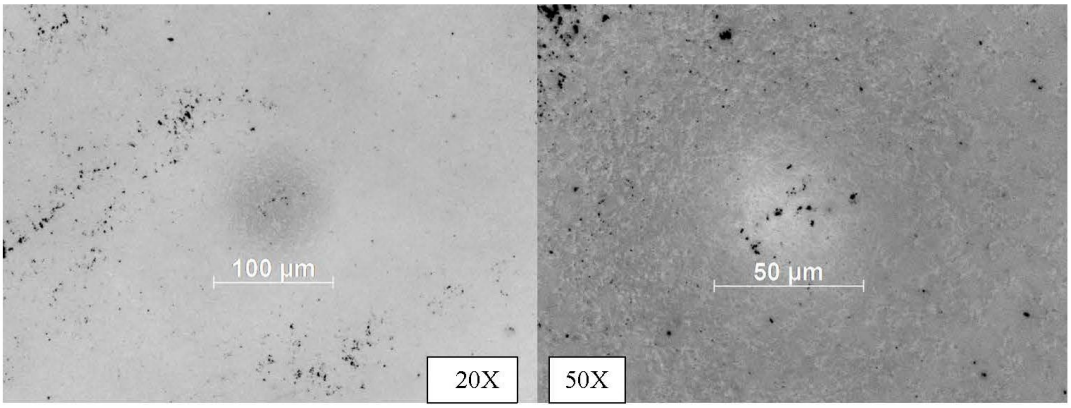

Fig. 66 TBF Face 2 images for 2VB063; left is at 20×, right is at 50×

Typical imaging for Specimen 2VB063's polished Face 1 appears in Fig. 67. The blotchy light and dark areas in the 5× image originated from residual BN film variations on the "far" Face 2, attenuating the transmitted beam strength while being imaged through Face 1. The quantum efficiency of the camera chip at 780 nm, coupled with the NIR camera's amplification function, exagerated those differences. The 10× RBF image on the right appears to show a white film-like surface. Magnifications above 10× failed to produce any usable micrographs for this face, either for TBF or RBF illumination.

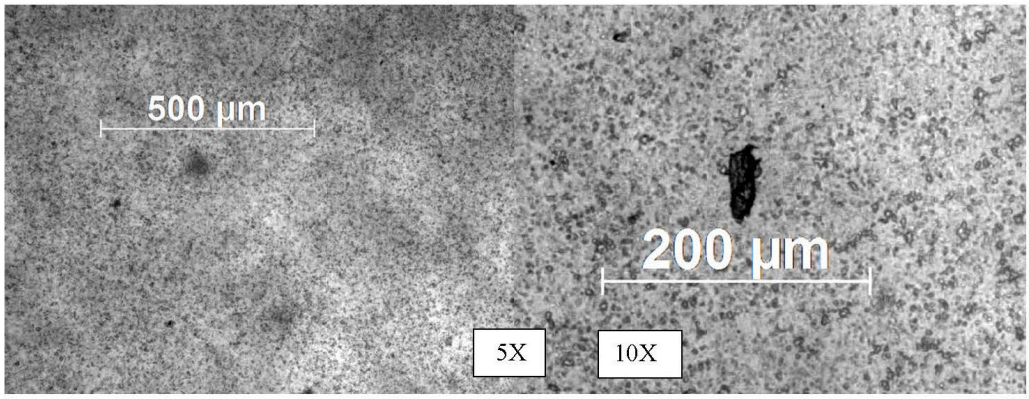

Fig. 67 (left) 2VB063's 780-nm, 5× TBF image showing both Face 1 and far Face 2, a result of the bulk nanocomposite transparency; (right) 10× RBF image was at magnification limit for Face 2

For 2VB063's polished Face 1, RBF white light easily captured the heavy black debris (Fig. 67) at 5×. At 20× (Fig. 68) the areas have no discernable BN. The finer features, while visible, appear less sharply defined. At higher magnifications the finer feartures blur rather than sharpen. The specimen's surface proved uneven when magnified.

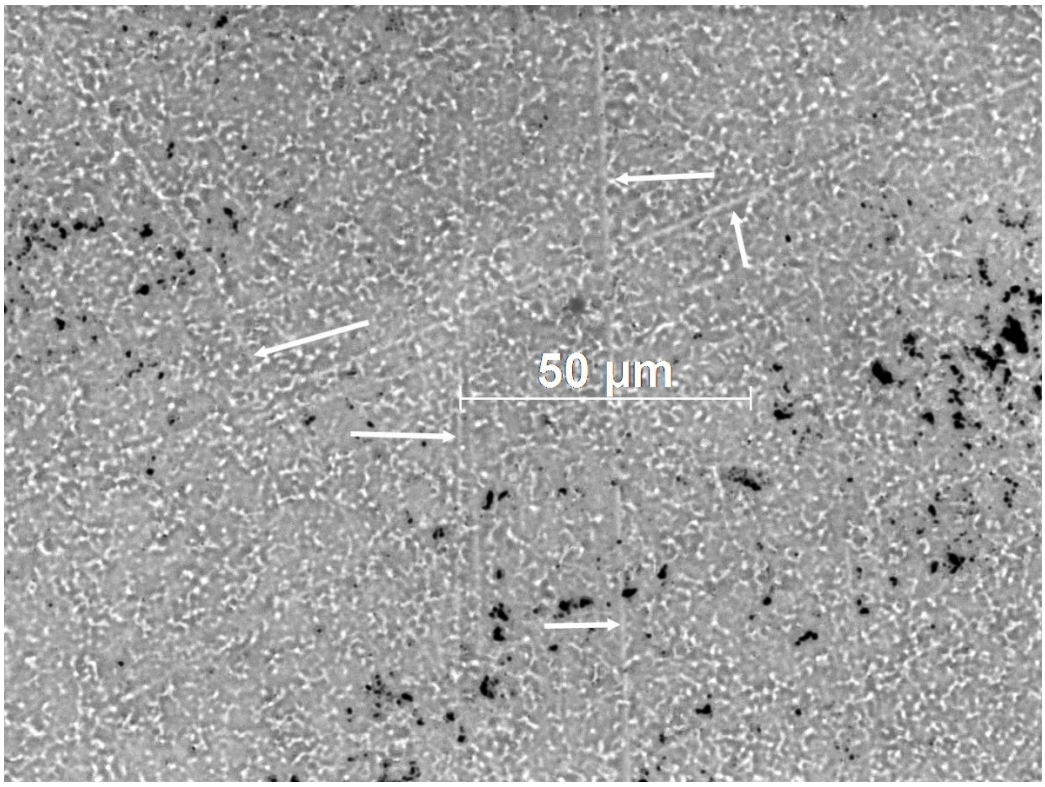

Fig. 68 At 20×, arrows mark debris agglomerations and grinding marks on 2VB063's Face 1, RBF

The most revealing finding was the apparent BN residue on polished surfaces, requiring EDX to confirm or refute those observations. Neither transmitted 780-nm nor 850-nm LED illumination revealed any subsurface structures in any specimen. Using reflected white light was more productive in producing analyzable images, but only for the faces. Reflected light proved to be a fast way to determine the condition of a postpolished specimen. For specimens with two polished faces, both faces are available to be examined. The drawback to two polished faces is not being able to image the nanocomposite proper. The available maximum magnification of 100× is too low for the nanosized phases of either species to be observed. Using a SEM requires one face be sacrificed to use conductive mounting material for mount attachment. The 780-nm LED having an emission spectrum pushing into the deep-red portion of the visible band, 400–700 nm, made checking the specimen edges for transmitted light exposure more reliable than with the 850-nm LED lamp or even the white-light LED.

6. Summary and Conclusions

Most usable imaging results used some mode of reflected white light and not transmitted NIR. The exclusion of the presence of subsurface interferents using

through-transmission of NIR was not accomplished in the manner originally anticipated as the suspect bodies are NIR opaque. The 780-nm illumination in several instances did demonstrate some transparency of a few specimens, while not revealing any of the apparent subsurface features observed in the 1× macro images, likely due to the light not penetrating far enough into the surface to observe a true feature.

The incoherent reflected-white-light-contrasting techniques proved effective for documenting polishing effects and any residual BN film on polished the hot-pressed specimens. Fully polished hot-pressed specimens that were tested appeared optically to retain some form of residual BN. The different white-light reflected light modes occasionally proved very effective at documenting the state of the surfaces, as in the case of Fig. 63, Section 5, capturing an apparent phase segregation.

RDF and reflected polarized light proved to be successful tools for quick nondestructive surveys. Past in-house attempts to use a confocal scope and visible wavelengths proved erratic with large-grain transparent ceramics, and the in-house unit does not possess any NIR sources. At the moment, there is no reliable optical method for subsurface studies of rare-earth-doped nanocomposites. While postprocessing with a third-party application could improve image quality, capturing more usable images at a compatible wavelength is the better solution, which is not possible with the current, in-house instrumentation.

Using Z-stacks in conjunction with RDF and the AxioVision multidimensional module, images revealed apparent roughness for a few polished specimens. In one instance, dark-field imaging readily demonstrated the nature of an agglomerate exposed by polishing and in another revealed pull-outs. At the time of capture, these results were not thought to add to the understanding of through-transmission of the specimens and were not explored in greater depth.

The use of incoherent NIR sources with a charge-coupled-device camera proved inadequate for achieving the present objective of clearly confirming or refuting subsurface obscurants in the translucent nanocomposite specimens. The absence of nonbiomedical research on microscopic imaging using NIR in the literature impeded rectifying the imaging issues. Application of broadband NIR in a standard optical system is currently too immature for use. Employing laser sources at an appropriate wavelength requires different sensors and light controllers, dictating the use of a different instrument similar to a confocal microscope. The latter will only work for those interferents opaque at the chosen wavelength, while the bulk material is transparent. For now, there appears to be no transmitted laser–NIR optical systems and application software designed for materials research. The

existing scanning-laser confocal microscopes designed for biomedical research can be adapted in part, but lack many material analysis applications. While not directly achieving its initial objective, the present work is a nice study on the effect of surface polishing on a variety of nanocomposite materials.

7. References

1. Fleischman Z, Blair V, Ku N, Merkle L, Moorehead C, Fry A, Kilczewski S, Harris D, Pavlacka R. Thermal property engineering: exploiting the properties of ceramic nanocomposites. Adelphi Laboratory Center (MD): Army Research Laboratory (US); 2018 Mar. Report No.: ARL-TR-8308.

2. Blair VL, Ku N, Brennan RE. Effect of batch-to-batch variability on the phase transition of precipitated erbium-doped alumina particles. Aberdeen Proving Ground (MD); Army Research Laboratory (US): 2017 Nov. Report No.: ARL-TR-8202.

3. Carl Zeiss MicroImaging GmbH. Oberkochen (Germany): Carl Zeiss MicroImaging GmbH; 2012 [accessed 2020 Jan 10]. https://www.zeiss.com/corporate/int/home.html.

4. Thorlabs, Inc. Newton (NJ): Thorlabs, Inc; 2020 [accessed 2020 Jan 10]. https://www.thorlabs.com.

5. Harris D. Zeiss Z2m microscope manual supplement, volume 1. Aberdeen Proving Ground (MD): CCDC Army Research Laboratory (US); 2019 Sep. Report No.: ARL-TN-0961.

6. Harris D. Subsurface optical microscopy of coarse grain spinels: phase 1. Aberdeen Proving Ground (MD): Army Research Laboratory (US); 2013 Dec. Report No.: ARL-TR-6732.

List of Symbols, Abbreviations, and Acronyms

3-D	three-dimensional
ARL	Army Research Laboratory
BN	boron nitride
CCDC	US Army Combat Capabilities Development Command
DSLR	digital single-lens reflex
EDX	energy dispersive X-ray
Er	erbium
HRm	high-resolution monochrome
IR	infrared
LED	light-emitting diode
MgO	magnesium oxide
NA	numeric aperture
NIR	rear-infrared
RBF	reflected bright field
RDF	reflected dark field
SEM	scanning electron microscope
TBF	transmitted bright field
wt%	weight percent
Y_2O_3	yttrium oxide

1 (PDF)	DEFENSE TECHNICAL INFORMATION CTR DTIC OCA
1 (PDF)	CCDC ARL FCDD RLD CL TECH LIB
3 (PDF)	CCDC ARL FCDD RLW ME V BLAIR S SILTON J SWAB